Journal of Rock Mechanics and Geotechnical Engineering xxx (xxxx) xxx

Contents lists available at ScienceDirect

Journal of Rock Mechanics and Geotechnical Engineering

journal homepage: www.jrmge.cn

Full Length Article

Revisiting the normal stiffness–permeability relations for shale fractures under true triaxial stress

Fudong Li [a], Derek Elsworth [b], Xia-Ting Feng [a], Tianyu Chen [a, c, d, *], Jun Zhao [a], Yingchun Li [e], Jianyu Zhang [f], Qiong Wu [g], Guanglei Cui [a, **]

[a] Key Laboratory of Ministry of Education on Safe Mining of Deep Metal Mines, School of Resources and Civil Engineering and Key Laboratory of Liaoning Province on Deep Engineering and Intelligent Technology, Northeastern University, Shenyang, 110819, China
[b] Department of Energy and Mineral Engineering, EMS Energy Institute and G3 Center, Pennsylvania State University, University Park, PA, 16802, USA
[c] State Key Laboratory of Coal Mine Safety Technology, China Coal Technology & Engineering Group Shenyang Research Institute, Shenfu Demonstration Zone, Shenyang, 113122, China
[d] National Energy Shale Gas R&D (Experiment) Center, Langfang, 065007, China
[e] State Key Laboratory of Coastal and Offshore Engineering, Dalian University of Technology, Dalian, 116024, China
[f] No. 3 Oil Production Plant of Daqing Oilfield Company Ltd, Daqing, 163113, China
[g] No. 4 Oil Production Plant of Daqing Oilfield Company Ltd, Daqing, 163511, China

ARTICLE INFO

Article history:
Received 12 November 2024
Accepted 6 January 2025
Available online xxx

Keywords:
Fracture permeability
Deformation
Fracture normal stiffness
True-triaxial stress
Principle of virtual work

ABSTRACT

Understanding the relationship between normal stiffness and permeability in rock fractures under high and true-triaxial in situ stress conditions is critical to assess hydro-mechanical coupling in the Earth's crust. Previous data on stiffness–permeability relations are measured under uniaxial stress states as well as under normal stress. However, many projects involve faulted formations with complex three-dimensional (3D) stress states or significant changes to the original stress state. We rectified this by following the permeability evolution using a true-triaxial stress-permeability apparatus as well as independently applying a spectrum of triaxial stresses from low to high. The relationship between permeability and fracture normal stiffness was quantified using constraints based on the principle of virtual work. The impacts of fracture-lateral and fracture-normal stresses on permeability and normal stiffness evolution were measured. It was found that permeability decreases with increasing fracture-lateral and fracture-normal stresses as a result of Poisson confinement, independent of the orientation of the fracture relative to the stresses. The lateral stresses dominated the evolution of normal stiffness at lower normal stresses (σ_3 = 10 MPa) and played a supplementary role at higher normal stresses (σ_3 > 10 MPa). Moreover, correlations between the evolution of permeability and normal stiffness were extended beyond the low-stiffness, high-permeability region to the high-stiffness, low-permeability region under high fracture-lateral stresses (10–80 MPa) with fracture-normal stress (10–50 MPa) conditions. Again, high lateral stresses further confined the fracture and therefore reduced permeability and increased normal stiffness, which exceeded the previous reported stiffness under no lateral stress conditions. This process enabled us to identify a fundamental change in the flow regime from multi-channel to isolated channelized flow. These results provide important characterizations of fracture permeability in the deep crust, including recovery from deep shale-gas reservoirs.

1. Introduction

Understanding the mechano-hydraulic coupling properties of rock fractures under confinements is essential in geological engineering applications, including in the recovery of hydrocarbons (Xue et al., 2020), the storage of CO_2 (Sun et al., 2024), and extraction of geothermal resources (Liu et al., 2022). Many deep and

* Corresponding author. Key Laboratory of Ministry of Education on Safe Mining of Deep Metal Mines, School of Resources and Civil Engineering and Key Laboratory of Liaoning Province on Deep Engineering and Intelligent Technology, Northeastern University, Shenyang, 110819, China.
** Corresponding author.
E-mail addresses: chentianyu@mail.neu.edu.cn (T. Chen), cuiguanglei@mail.neu.edu.cn (G. Cui).

https://doi.org/10.1016/j.jrmge.2025.01.007
1674-7755/

subsurface engineering projects involving fluid-flow are conducted under high in situ stress conditions (Raziperchikolaee and Pasumarti, 2020; Jia et al., 2021; Kruszewski et al., 2022; Yong et al., 2022). Moreover, the formations in these deep-subsurface conditions may be strongly compressional and critically stressed, and reverse faults are included (Yong et al., 2022). The stress state in these terranes will reflect reverse-faulting stress regimes ($\sigma_{hmax} > \sigma_{hmin} > \sigma_v$, where σ_v is the vertical stress and σ_{hmax} and σ_{hmin} are the maximum and minimum principal horizontal in situ stresses, respectively) (Fan et al., 2019). For example, the recovery of shale gas from tight reservoirs is shown in Fig. 1. Fracture deformability (characterized as fracture stiffness) is fundamentally related to permeability, which allows for characterizing hydro-mechanical coupling properties in the deep crust (Li et al., 2021a). The permeability of low permeable formations is dominated by fractures and strongly dependent on stresses (Liu et al., 2009; Cui et al., 2020a; Jiang et al., 2021; Chen et al., 2023). In summary, fracture permeability and stiffness are dominated by in situ stress state. While most measurements have been confined to the hydrostatic ($\sigma_1 = \sigma_2 = \sigma_3$, where σ_1, σ_2, and σ_3 are the maximum, intermediate, and minimum principal stresses, respectively) or simple triaxial ($\sigma_1 > \sigma_2 = \sigma_3$) stress states, the evolution of the relationship between stiffness and permeability under complex three-dimensional (3D) stress states ($\sigma_1 > \sigma_2 > \sigma_3$) remains poorly understood.

Previous experimental studies have not only explored the impact of stress on matrix permeability, but also paid attention to fracture permeability because fractures serve as the principal flow channel in low-permeability formations (Cho et al., 2013; Tan et al., 2019; Zhang et al., 2019; Liu et al., 2023). The permeability of rocks with fractures is sensitive to variations in stress (Dong et al., 2010), with this stress leading to large variations in stiffness (Petrovitch et al., 2013, 2014). Fracture permeability decreases with increasing stiffness and stress, which allows permeability evolution to be exponentially related to variations in stress (Pan et al., 2015; Cui et al., 2018; Ogata et al., 2022). Furthermore, fracture permeability shows a rapid decrease under low stress and a slower decrease under high stress (Chen et al., 2019a; Zhou et al., 2019). However, most studies are performed under conventional triaxial stress conditions ($\sigma_1 > \sigma_2 = \sigma_3$), which lacks the impact of intermediate principal stress on the permeability evolution of deeper rocks (Haimson and Chang, 2002; Xie et al., 2022). A variety of characterizations have defined the evolution of permeability as a function of stress through the compressibility of the fractures that comprise the representative elementary volume (REV) (Li and Liu, 2021; Li et al., 2021b).

At the field scale, the evolution of stress and flow paths in deep subsurface reservoirs is remotely monitored using electrical and electromagnetic geophysical sensing methods, thus enhancing our understanding (Johnson et al., 2021, 2024). The complex interaction between fracture deformation and effective stresses that are induced by oil and gas production allows the mechanical response of the fracture to exhibit normal closure and/or shear behavior. Stress-dependent fractures involve a coupling mechanism between closure, shear, and fluid flow, respectively (Barton et al., 1985; Lei and Barton, 2022). Previous works (e.g. Gutierrez et al., 2000; Carey et al., 2015; Frash et al., 2016; Ye and Ghassemi, 2019, 2020; Meng et al., 2022) have investigated the coupled hydro-mechanical properties of shear fracture in rock under normal and shear loading using the triaxial direct-shear method. The ability to characterize shear slip on natural fractures and faults could enable us to better predict the risk of induced seismic activity (Ellsworth et al., 2019). Barton (2020) proposed shear-dilation-flow coupling mechanisms in rock fracture shear processes in consideration of joint roughness coefficient (JRC). In addition, Longmaxi shale fractures have been conducted with coupled friction-permeability experiments with the aim of exploring the relationships between fracture slip and permeability evolution under various shear velocity conditions (Jia et al., 2020; Cui et al., 2024). However, while many modelling studies assume that fracture-normal and shear stiffness are equal, extensive laboratory and field measurements have shown that normal stiffness is commonly much greater than shear stiffness (Bandis et al., 1983; Verdon and Wüstefeld, 2013; Choi et al., 2014). Thus, understanding the stress–closure–flow coupling

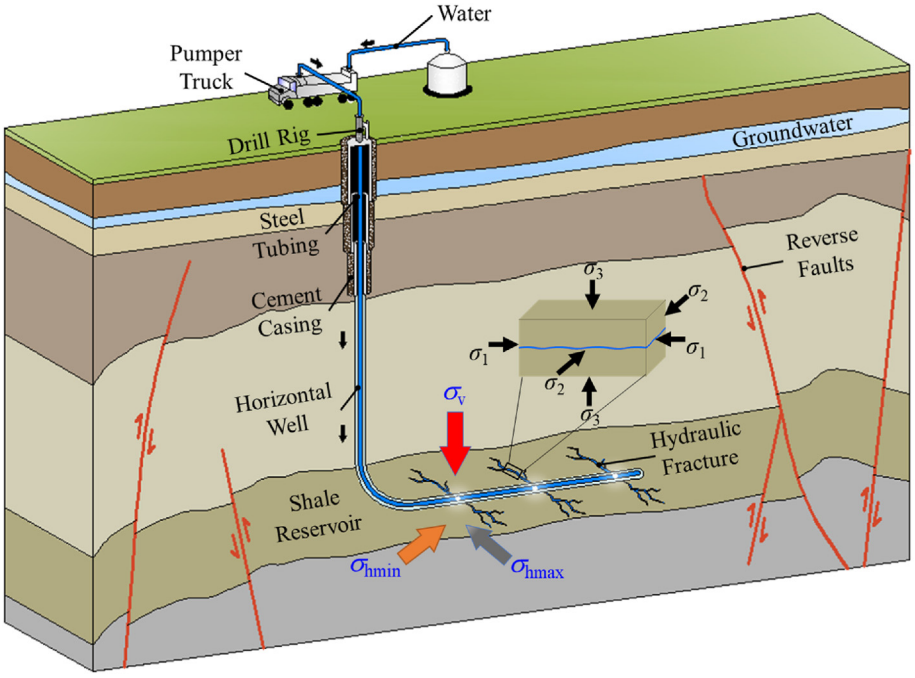

Fig. 1. Schematic illustration of stimulated reservoir volume.

mechanisms in rock fractures is of interest for various geo-engineering applications. Previous studies (e.g. Guglielmi and Mudry, 2001; Cappa et al., 2008) have determined hydraulic aperture and fracture normal stiffness from field tests that have measured fluid pressure and mechanical displacement; however, field tests that can simultaneously measure hydro-mechanical responses in fractures are relatively rare.

Many previous studies have focused on the hydro-mechanical behavior of fractured rocks via laboratory tests of single deformable fractures. A spring model characterized by fracture normal stiffness (Rutqvist, 1995; Jiang et al., 2009) has been proposed for describing the behavior of permeability with stress and for assessing the impact of fracture deformability on permeability evolution (Pyrak-Nolte and Morris, 2000; Thörn et al., 2014; Li et al., 2021a). Fracture normal stiffness is strictly related to fracture geometric characteristics, such as fracture aperture (Pyrak-Nolte, 1996; Petrovitch et al., 2014). Therefore, a good understanding of normal stiffness with varied fracture apertures is vital when it comes to predicting the evolution of fracture permeability more accurately. Significant advances have recently been made in this area (Raven and Gale, 1985; Zimmerman et al., 2004; Walsh et al., 2008; Petrovitch et al., 2013). In a conventional approach, normal stiffness is directly obtained through fracture deformation. A hyperbolic law (Bandis et al., 1983; Packulak et al., 2021) that relates fracture stiffness to fracture deformation provides a positive correlation between normal stiffness and applied stress. Additionally, a negative correlation exists between normal stiffness and permeability (Pyrak-Nolte, 1996; Jiang et al., 2009; Wang and Cardenas, 2016; Zou and Cvetkovic, 2020) under normal stress that allows hydro-mechanical coupling (Li et al., 2008, 2015, 2021a) of fractures to be established via the relationship between stiffness and permeability. Well-mated fractures show a weak dependence of permeability on normal stiffness (Pyrak-Nolte and Morris, 2000; Thörn et al., 2014), although the dependence on fracture-lateral stress remains ill-defined. Furthermore, the relationship between normal stiffness and permeability that was investigated in these studies was centered on the low-stress, high-permeability region, with limited data being reported for high-stress, low-permeability region.

Existing investigations on permeability evolution and relationship between normal stiffness and permeability have been mainly limited to uniaxial or conventional triaxial stress conditions (Pyrak-Nolte and Morris, 2000; Thörn et al., 2014; Chen et al., 2015; Cui et al., 2020b; Li et al., 2021a), whereas practical projects typically experience true-triaxial stress conditions (Puller et al., 2016; Chen et al., 2019b; Lu et al., 2019b; Zhao et al., 2023). Therefore, the effects of the fracture-lateral stress on permeability and fracture normal stiffness remain indeterminate. In the present study, permeability and deformation measurements of shale that contained a single fracture were conducted under true-triaxial stress conditions. Fracture normal stiffness was determined using the principle of virtual work. In the text, the relationship between permeability and normal stiffness, as well as the mechanism underlying permeability evolution under true-triaxial stress conditions, was defined and discussed.

2. Experimental apparatus and methodology

2.1. Sample preparation

The shale samples used in the present study were obtained from an outcrop of the Silurian Longmaxi Formation in the Sichuan Basin, China. As shown in Fig. 2, many reverse faults are developed in the study area (Nie et al., 2020). A large shale block was cut into prismatic samples of 50 mm × 50 mm × 100 mm (length × width × height) along the direction of the bedding strike. The study involves an artificially fractured shale sample (AFS) and an intact shale sample (IS), as shown in Fig. 2b. The AFS in the study contained a preformed and fully penetrated single fracture. The standard shale sample was split along the bedding in order to create a horizontal tension fracture that was flat, smooth, and well-matched. The sample was broken into two halves along the penetrated fracture and was then carefully put together. Table 1 defines the mineral composition and organic carbon content (TOC) together with the maturity ($R_{o,max}$) of the shale samples. True-triaxial stress-permeability tests were conducted on the AFS with a single bedding-parallel fracture in order to determine the influence of the maximum, intermediate, and minimum principal stresses on stiffness and permeability evolution. In order to quantify matrix deformation and separate fracture-normal deformation, additional true-triaxial compression tests are performed with the IS (see Fig. 2b) that has been sampled from the same shale block as the AFS.

2.2. Experimental apparatus and testing procedure

As shown in Fig. 3, a true-triaxial stress-permeability cell used in the tests comprises a combined true-triaxial compression testing apparatus (Feng et al., 2018) (Fig. 3b) with a permeability testing device (Fig. 3a). We applied stress and measured strain and permeability under true-triaxial stress conditions. Permeability testing was performed via upstream injection systems (UIS) into downstream injection systems (DIS), which comprised pressure-regulating and sensing components and tubing. Two Keller pressure sensors were installed on the permeability testing device to monitor gas pressures in the UIS and DIS with a measuring range of 0–20 MPa and accuracy of 0.05%. A differential pressure sensor (Keller) was installed between the UIS and DIS to monitor the gas pressure difference. The measuring range and accuracy of the differential pressure sensor are 0–1 MPa and 0.1%, respectively. The UIS and DIS were connected to the loading platens that were mounted on the integrated seepage fixture (ISF) in order to enable the fluid throughflow experiments.

The interlocked ISF fully contacted the four surfaces of the sample in order to generate a uniformly distributed stress as well as to eliminate loading gaps and fluid short-circuiting effects (Zhao et al., 2022). The design of the ISF is depicted in Fig. 4a. The inner surface of the ISF was designed as a plane with a square lattice seepage channel. Overlapping platens comprised the inner surface of the ISF, which ensured that the corners of the sample were sealed during rock compression and seepage. External thread fittings were combined with a copper gasket in order to seal the converted interface on the ISF. As shown in Fig. 4b, the free surface of the sample in the σ_3 direction and the sealing area at the four corners of the ISF are sealed with a sealant.

As shown in Fig. 3d, the ISF was mounted at the geometric center of the stress-loading seepage platform after the sample had been installed. Subsequently, two converted interfaces of the fluid seepage channel on the left and right parts of the ISF related to two internal interfaces of the seepage channel reserved by the seepage module through the compressible seepage coil. Next, rigid loading blocks were placed on the top/bottom and left/right sides of the ISF. During the test, the maximum (σ_1), intermediate (σ_2), and minimum (σ_3) principal stresses were applied independently. The σ_1 and σ_2 were applied by rigid loading, and σ_3 was flexibly loaded by the hydraulic oil in the pressure chamber driven by the loading pump. Deformations in σ_1 and σ_2 directions were measured using LVDTs, with deformation in σ_3 direction achieved through a U-shaped “beam strain gauge.” The linear variable differential transducers (LVDT) and U-shaped sensors were calibrated using

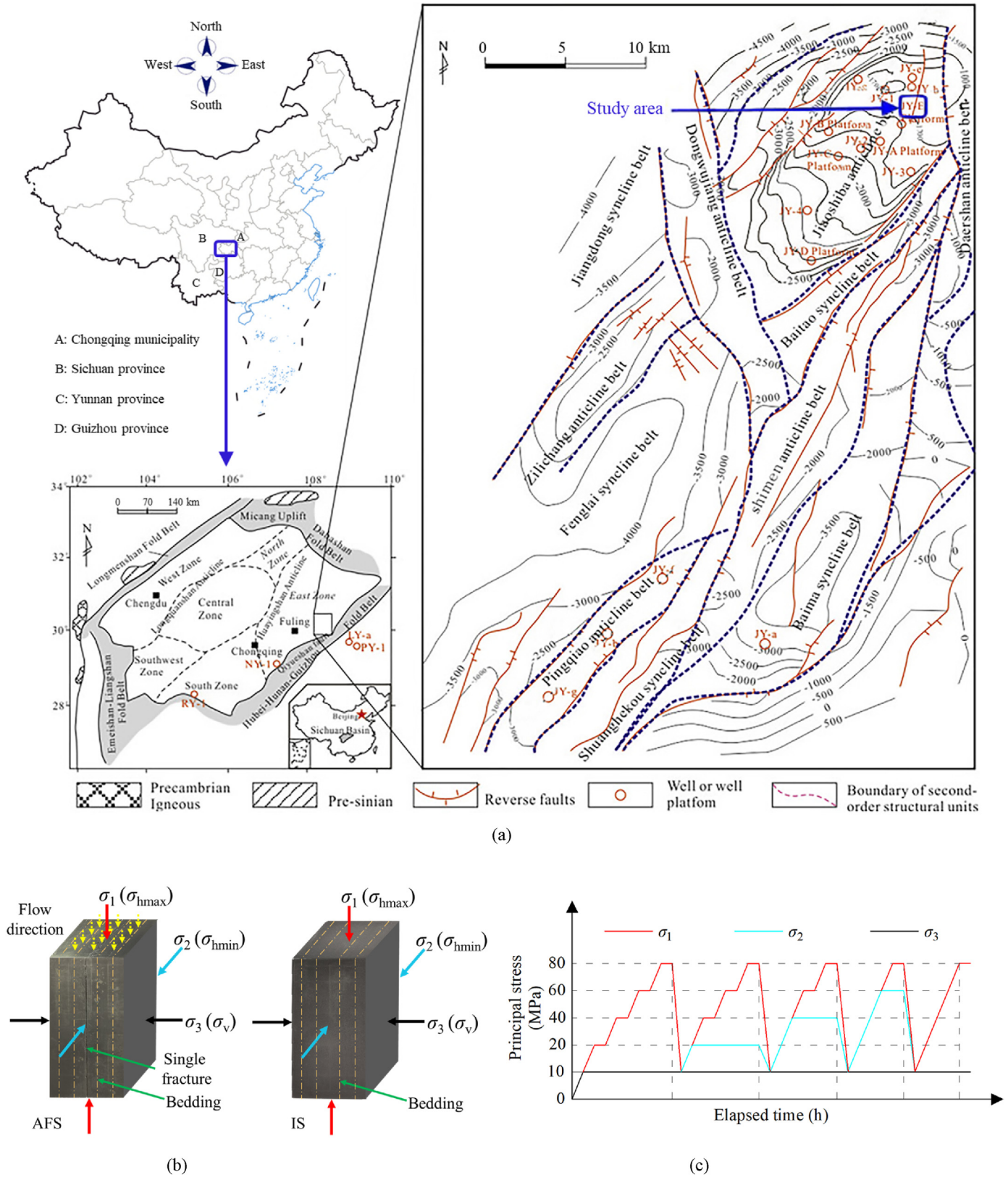

Fig. 2. Geologic setting, stress loading path, and orientation of stresses: (a) Structural map of the Longmaxi Formation (modified after Nie et al. (2020)), (b) relative orientations of principal stresses and fluid flow in a fully penetrated fracture after splitting of AFS (σ_3 perpendicular to the fracture, σ_1 and σ_2 parallel to the fracture) and relative orientations of principal stresses and bedding plane of IS, and (c) stress loading path when $\sigma_3 = 10$ MPa.

Table 1
Geochemical properties of the shale samples.

Mineral composition (%)							$R_{o,max}$ (%)
Quartz	Feldspar	Pyrite	Clay minerals	Calcite	Dolomite	TOC	
32.45	3.43	3.13	18.57	32.16	8.02	2.24	2.41

Table 2
Three-dimensional stress states under each test stage.

Shale	σ_3 (MPa)	σ_2 (MPa)	σ_1 (MPa)
Artificially fractured shale sample	10	10, 20, 40, 60, 80	10, 20, 40, 60, 80
	20	20, 40, 60, 80	20, 40, 60, 80
	40	40, 60, 80	40, 60, 80
	50	50, 60, 80	50, 60, 80
Intact shale sample	10	10, 20, 40, 60, 80	10, 20, 40, 60, 80
	20	20, 40, 60, 80	20, 40, 60, 80
	40	40, 60, 80	40, 60, 80
	50	50, 60, 80	50, 60, 80

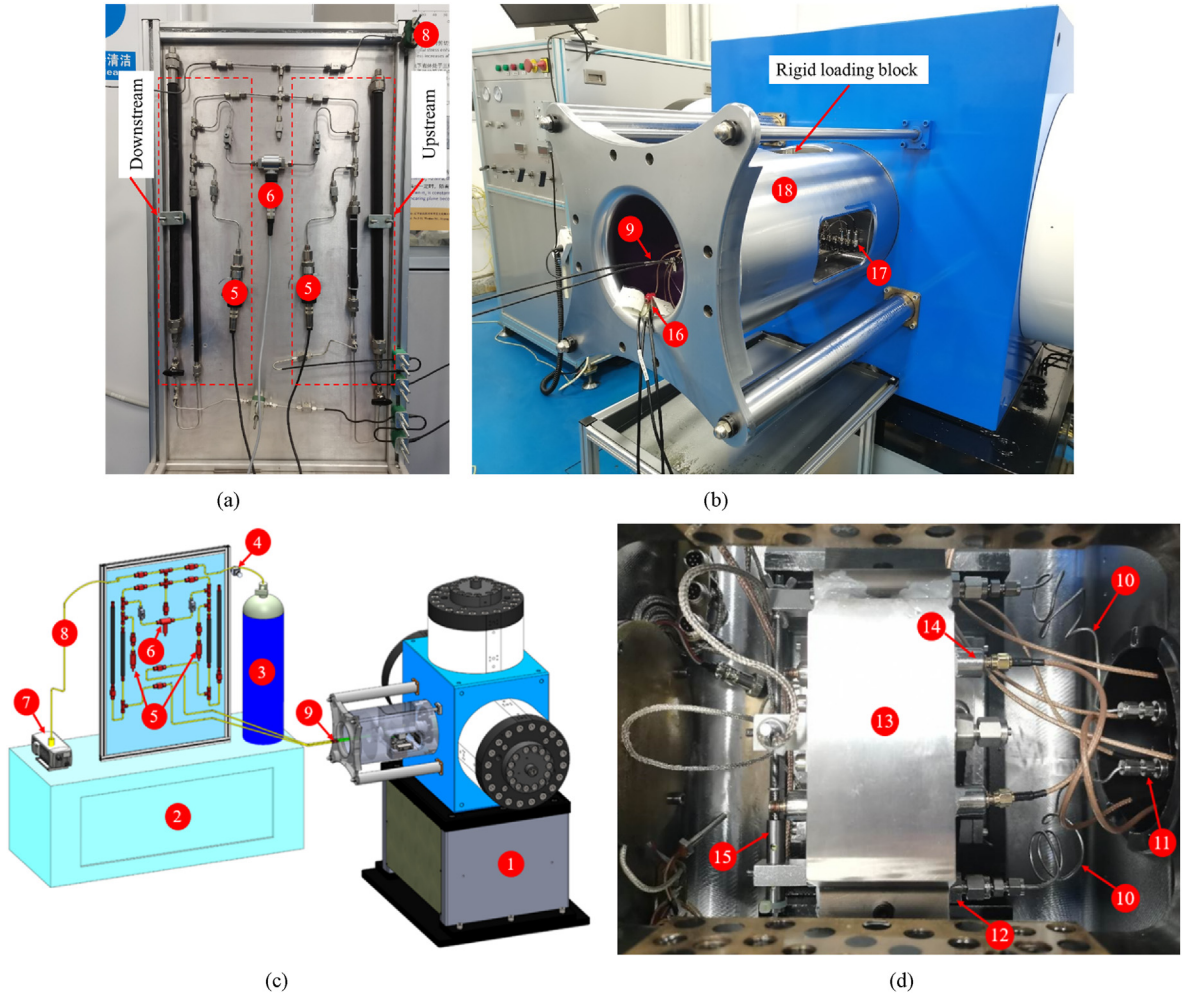

Fig. 3. True-triaxial stress-permeability cell: (a) Permeability testing device, (b) true-triaxial compression testing apparatus, (c) overall structure, and (d) top view of the seepage module. 1. true-triaxial compression testing apparatus; 2. permeability testing device; 3. gas cylinder; 4. pressure reducing value; 5. pressure sensor; 6. differential pressure sensor; 7. vacuum pump; 8. tubing; 9. external interface; 10. compressible seepage coil; 11. internal interface; 12. converted interface; 13. ISF; 14. acoustic emission sensor; 15. LVDT deformation sensor; 16. AE aviation connector; 17. LVDT aviation connector; 18. stress-loading seepage platform.

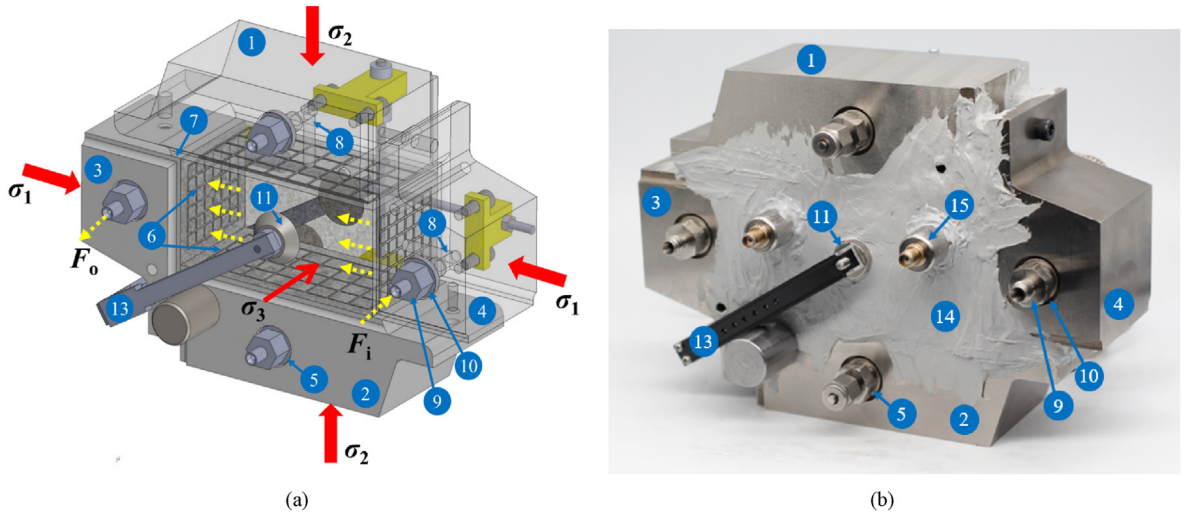

Fig. 4. Schematic and photograph of the integrated seepage fixture (ISF): (a) Schematic of the ISF, and (b) photograph of the ISF. 1. upper seepage fixture; 2. lower seepage fixture; 3. left seepage fixture; 4. right seepage fixture; 5. converted interface; 6. square lattice seepage channel; 7. overlapping platen; 8. internal seepage channel of the seepage fixture; 9. external thread fitting; 10. copper gasket; 11. strain gasket; 12. LVDT deformation sensor; 13. U-shaped sensor; 14. sealant; 15. acoustic emission sensor.

a micrometer caliper in order to achieve an accuracy of 0.1%. A detailed description of stress loading and deformation measurement is available in Feng et al. (2018).

2.3. Stress and gas pressure paths

A series of true-triaxial stress-permeability tests are conducted under different stress conditions using the stress path illustrated in Fig. 2c. The evolving permeability was obtained by applying multiple loading and unloading cycles. Currently, shale gas resources are under development in China at depth of <3500 m, particularly in the Longmaxi Formation in the Sichuan Basin (Li et al., 2022). Therefore, the maximum principal stress was set to 80 MPa for a vertical in situ stress gradient of ~25 MPa/km (Chen et al., 2019b). According to Fig. 2a, reverse faults in the study area are widely distributed (Nie et al., 2020). Reverse-faulting stress regimes ($\sigma_{hmax} > \sigma_{hmin} > \sigma_v$) were determined using the Andersonian stress regimes proposed by Anderson (1905). In addition, based on in situ stress measurements and analysis of the Longmaxi shale formation (Yong et al., 2022), the stress state near some faults was found to transition from a strike-slip ($\sigma_{hmax} > \sigma_v > \sigma_{hmin}$) to a reverse ($\sigma_{hmax} > \sigma_{hmin} > \sigma_v$) faulting stress regime. Thus, the vertical stress $\sigma_v = \sigma_3$ and the maximum σ_{hmax} and minimum σ_{hmin} principal horizontal in situ stresses are σ_1 and σ_2, respectively, based on a reverse-faulting stress regime ($\sigma_{hmax} > \sigma_{hmin} > \sigma_v$). Furthermore, σ_v is typically perpendicular to the direction of the bedding for shale reservoirs. The stress loading and fluid-flow orientations are set as shown in Fig. 2b (where $\sigma_3 = \sigma_v$ is perpendicular to the bedding plane of the single fracture and seepage was within this fracture).

Four minimum principal stress stages (σ_3 = 10 MPa, 20 MPa, 40 MPa, and 50 MPa) were set for the true-triaxial seepage tests. Taking the minimum principal stress of 10 MPa shown in Fig. 2c as an example, the stress path of the loading and unloading cycles is set as follows:

(1) The sample is loaded to a hydrostatic stress of $\sigma_1 = \sigma_2 = \sigma_3 = 10$ MPa at a stress-loading rate of 0.1 MPa/s. Then, the maximum and intermediate principal stresses are simultaneously increased from 10 MPa to 20 MPa at a rate of 0.5 MPa/s through the stress path shown in Fig. 2c.
(2) The maximum principal stress was gradually increased to 80 MPa in 20-MPa increments before finally unloading back to the initial value of 10 MPa. The loading paths to the remaining levels of σ_2 ($\sigma_2 = 10$ MPa, 40 MPa, 60 MPa, and 80 MPa) and σ_3 ($\sigma_3 = 20$ MPa, 40 MPa, and 50 MPa) were the same as before. The stress states for each permeability test stage are listed in Table 2. It should be noted that two permeability tests in the initial stress state ($\sigma_1 = \sigma_2 = \sigma_3 = 10$ MPa) were conducted in order to overcome the impact of compaction effects.
(3) The second permeability result (0.14 mD) is significantly smaller than the first one (0.24 mD) and is finally identified as the data for the initial stress state shown in Fig. 5a, which indicates that the fracture is compacted. Furthermore, the true-triaxial stress tests of the IS were performed under the same stress path as the AFS.
(4) Non-sorptive nitrogen gas was used as the permeating fluid in the present study. The gas pressure at the UIS was set to 1 MPa, with a value of 0 MPa specified for the DIS and the pulse-decay method used.

2.4. Permeability testing

The permeability testing device and sample had been vacuum-saturated before gas was injected into the closed UIS and DIS at a defined differential (~1 MPa) (Chen et al., 2021). Next, the UIS and DIS valves were opened simultaneously, transient gas pressures were recorded over elapsed time, and the valves were then closed as the upstream and downstream gas pressures equilibrated. Permeability was measured by the pulse-decay method as (Brace et al., 1968; Ma et al., 2016; Tan et al., 2017):

$$\frac{P_u - P_d}{P_{u,0} - P_{d,0}} = e^{-\alpha t} \tag{1}$$

where P_u–P_d is the pressure difference between the upstream (UIS) and downstream injection systems (DIS) at time t, $P_{u,0}$–$P_{d,0}$ is the pressure difference between the UIS and DIS in the initial stage, and α is the pressure-decay exponent. The measured permeability k can be obtained via α as (Brace et al., 1968; Tan et al., 2018):

$$k = 2\mu L\alpha \Big/ \left[A_1 (P_{u,0} + P_{d,0}) \left(\frac{1}{V_u} + \frac{1}{V_d}\right)\right] \tag{2}$$

where A_1 is the cross-sectional area of the sample in the σ_1 direction; L is the sample length; μ is the viscosity of the flowing fluid; and V_u and V_d are the volumes of the UIS and DIS, respectively.

3. Results

3.1. Evolution of permeability with principal stress

Fig. 5a presents the results of the permeability and principal strain of the AFS under different stress regimes. The permeability at different principal stresses that correspond to those in Fig. 5a is shown in Fig. 5b (σ_3 = 10 MPa) and c (σ_3 = 20 MPa, 40 MPa, and 50 MPa), respectively. With increasing σ_1, σ_2, σ_3, and volumetric strain ε_v, the permeability gradually decreased by varying degrees. As shown in Fig. 5b and c, with increasing σ_2 and σ_1, the permeability rebounds when the sample is unloaded to the initial hydrostatic stress states of $\sigma_1 = \sigma_2 = \sigma_3 = 10$ MPa, 20 MPa, 40 MPa, and 50 MPa. However, the permeability exhibited significant hysteresis at the same hydrostatic pressure both before and after loading and unloading. This permeability hysteresis would be induced by irrecoverable deformation of the fracture by loading of σ_1 and σ_2. For example, the difference in permeability between the initial state and the state after the first stress cycle (both under the same conditions of $\sigma_1 = \sigma_2 = \sigma_3 = 10$ MPa) was 0.102 $\times$ 10^{-1} mD.

3.2. Effect of maximum, intermediate, and minimum principal stresses on permeability and strain

Fig. 6 displays the variations in the permeability and principal strain of the AFS with σ_1, σ_2, and σ_3 for different 3D stress conditions. Permeability is decreased by varying degrees with increasing σ_1, σ_2, and σ_3, as shown in Fig. 6a–c. For example, at σ_3 = 10 MPa and σ_2 = 20 MPa, permeability was decreased by ~50% from σ_1 = 20 MPa to σ_1 = 80 MPa. While for σ_3 = 10 MPa and σ_1 = 80 MPa, permeability was found to decrease from σ_2 = 20 MPa to σ_2 = 80 MPa by 68.79%. Moreover, permeability was decreased by 63.32% from σ_3 = 10 MPa to σ_3 = 50 MPa (σ_2 = 60 MPa, σ_1 = 80 MPa). Only some typical data are shown here because the observations under other stress conditions are similar. These observations reveal that the intermediate principal stress has a similar effect to σ_1 on permeability evolution. The single fracture was compressed and closed with increasing σ_2 or σ_1, which significantly decreased the permeability. Therefore, the effect of σ_2 on permeability was significant and could not be ignored; while direct compression and closure of the fracture due to increased fracture-normal stress (σ_3) under the constraint of σ_2 and σ_1 offered a reasonable explanation for the decreased permeability.

Furthermore, Fig. 6 shows the variations in the maximum principal strain ε_1, intermediate principal strain ε_2, and minimum principal strain ε_3 with σ_1 (Fig. 6a), σ_2 (Fig. 6b), and σ_3 (Fig. 6c)

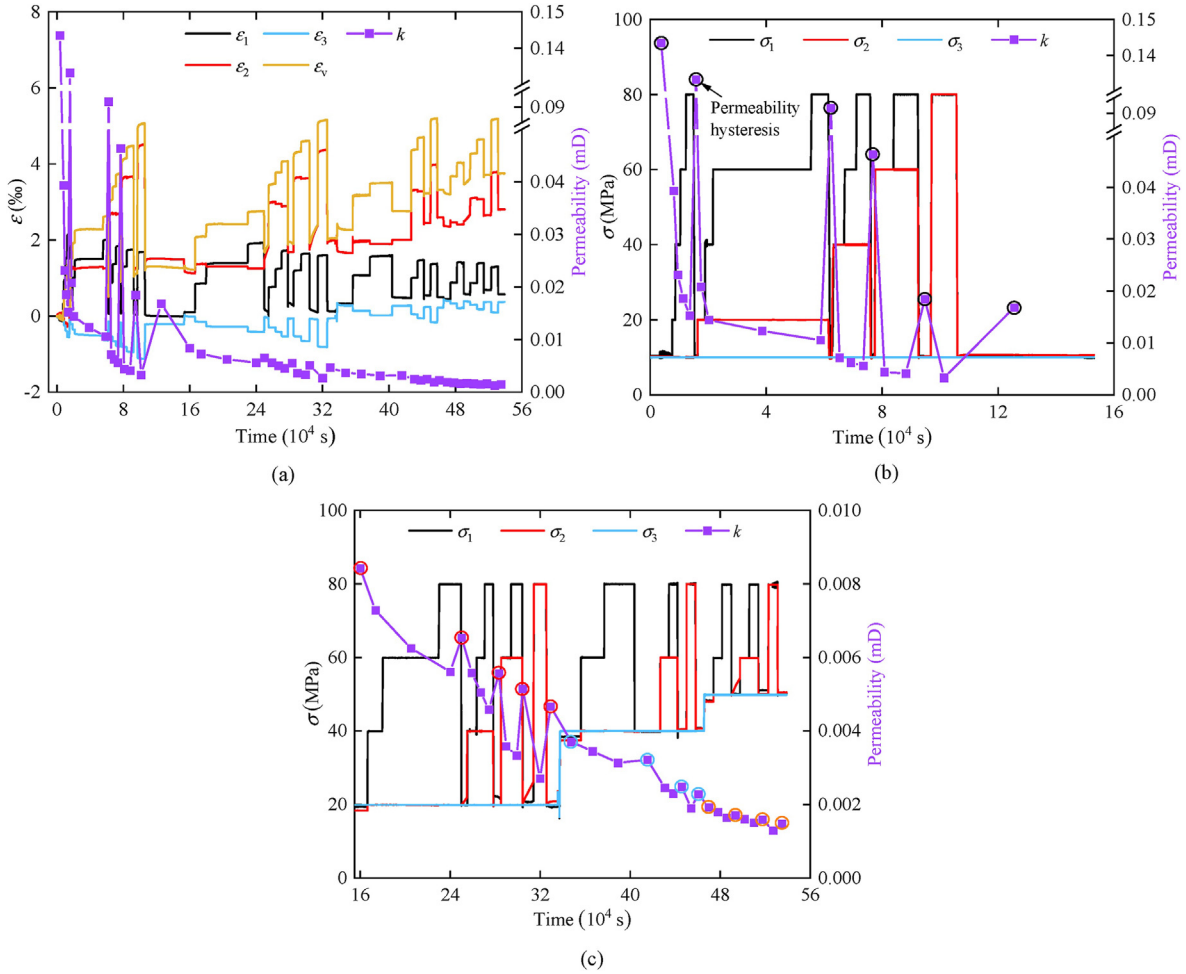

Fig. 5. Permeability and principal strains of artificially fractured shale sample under different stress conditions: (a) Permeability and principal strain under all tested stress conditions, (b) permeability at σ_3 = 10 MPa, and (c) permeability at σ_3 = 20 MPa, 40 MPa, and 50 MPa.

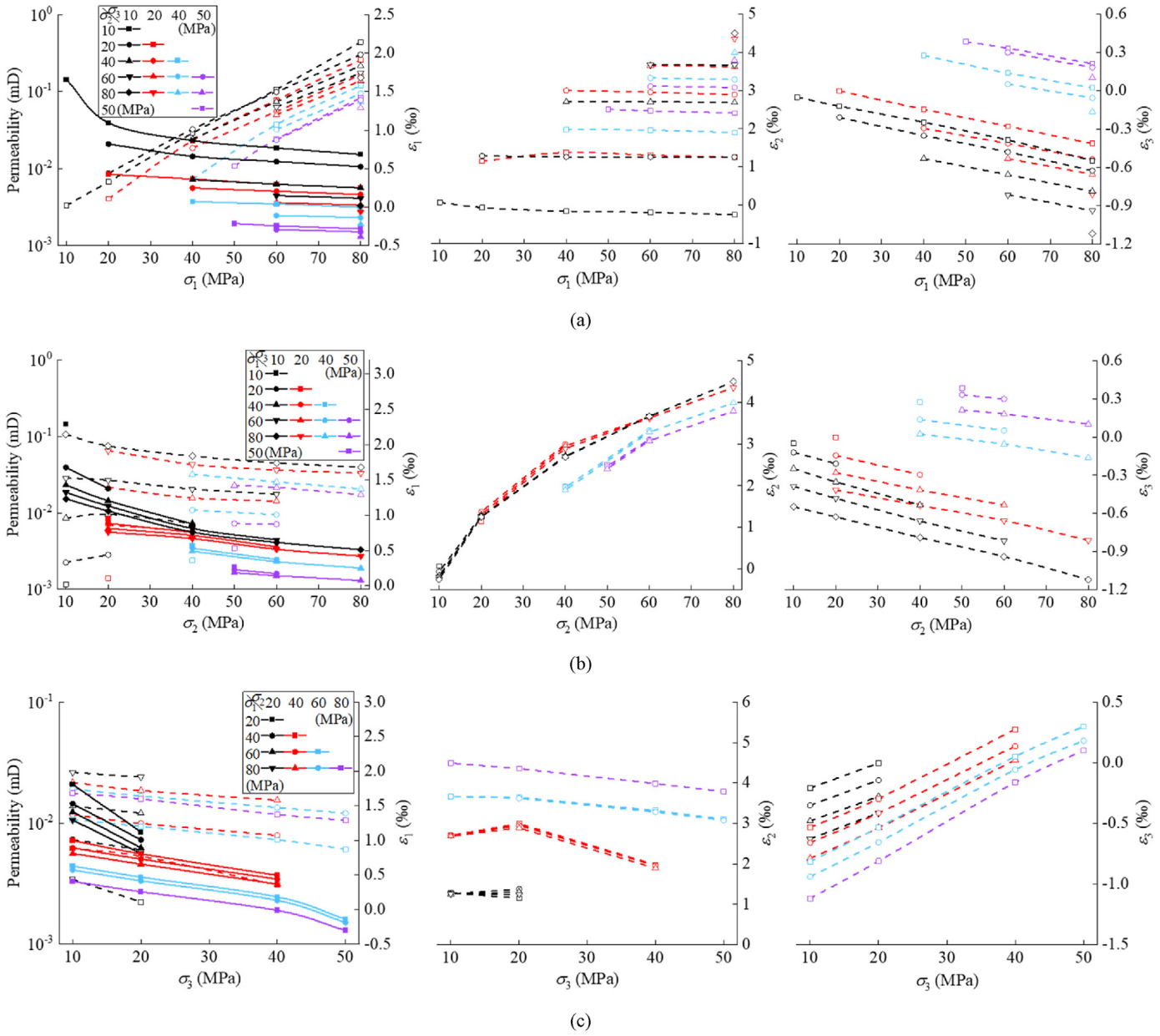

Fig. 6. Variations in the permeability and principal strain of the artificially fractured shale sample with σ_1, σ_2, and σ_3 for different 3D stress conditions: (a) Permeability, ε_1, ε_2, and ε_3 as a function of σ_1; (b) permeability, ε_1, ε_2, and ε_3 as a function of σ_2; and (c) permeability, ε_1, ε_2, and ε_3 as a function of σ_3. Solid symbols and solid line: permeability under different stress conditions; open symbols and dashed line: principal strain under stress conditions corresponding to the solid symbols.

under different 3D stress conditions. It should be emphasized that the LVDT deformation sensor was calibrated as positive in compression and as negative in expansion – that is, the sample was compressed when ε increased, and vice versa. The changes in the values of ε_1, ε_2, and ε_3 were reported as $\Delta\varepsilon_1$, $\Delta\varepsilon_2$, and $\Delta\varepsilon_3$, respectively, while the change in volumetric strain ε_v was defined as $\Delta\varepsilon_v = \Delta\varepsilon_1 + \Delta\varepsilon_2 + \Delta\varepsilon_3$. Fig. 6 reveals that ε_1 gradually increases with increasing σ_1, whereas ε_2 and ε_3 gradually decreases as σ_1 increases due to the Poisson effect. For example, when $\sigma_3 = 10$ MPa and $\sigma_2 = 20$ MPa, ε_1 was increased by 1.542‰, ε_2 and ε_3 were decreased by 0.032‰ and 0.418‰, respectively, as σ_1 increased from 20 MPa to 80 MPa, resulting in a 1.092‰ increase in ε_v. As illustrated, deformation was dominated by compression in σ_1 direction and by expansion in σ_3 direction, while expansion in σ_2 direction was insignificant, which caused $\Delta\varepsilon_v$ to always be positive as σ_1 increased. Compared with the effect of σ_1 on deformation, ε_3 and ε_1 gradually decreased, and ε_2 increased with increasing σ_2. For example, as σ_2 increased from 20 MPa to 80 MPa ($\sigma_3 = 10$ MPa, $\sigma_1 = 80$ MPa), ε_2 was increased by 3.238‰ while ε_1 and ε_3 were decreased by 0.302‰ and 0.492‰, respectively, which resulted in a 2.444‰ increase in ε_v. The sample deformation caused by increased σ_2 always showed compression in σ_2 direction, expansion in σ_3 and σ_1 directions, and a final positive volumetric strain increment. As illustrated, with increasing σ_3, ε_3 increased while ε_2 and ε_1 decreased for different σ_2 and σ_1 values, which indicates that the sample had compacted in σ_3 direction and expanded in σ_2 and σ_1 directions. The increased volumetric strain also indicated that the sample had been gradually compressed with increasing three principal stresses, and the internal volume that had been compressed was primarily of single fracture. Consistent observations

were also found for other strains ε_1, ε_2, ε_3, and ε_v. These deformation characteristics represent the orthotropic nature of the deformation moduli of the shale matrix.

As shown in Fig. 6, when depicting permeability results under all stress conditions, permeability is found to decrease from the initial to the final stress state with increasing σ_1, σ_2, and σ_3 on the order of 6%–89%, 11%–78%, and 44%–64%, respectively. This behavior indicates that the effects of σ_1, σ_2, and σ_3 on permeability were differentiated for different lateral constraints.

3.3. Permeability response to mean stress and stress difference

Fig. 7 presents the relationship between permeability on one hand and the mean stress and intermediate principal stress coefficient for different 3D stress conditions on the other hand. In the present study, the permeability evolution of the AFS in the true-triaxial stress states – which ranged from triaxial compression ($\sigma_1 > \sigma_2 = \sigma_3$) to triaxial extension ($\sigma_1 = \sigma_2 > \sigma_3$) – was investigated under certain stress conditions. The mean stress (p) and intermediate principal stress coefficient (b) were defined as functions of σ_1, σ_2, and σ_3:

$$p = \frac{\sigma_1 + \sigma_2 + \sigma_3}{3} \tag{3}$$

$$b = \frac{\sigma_2 - \sigma_3}{\sigma_1 - \sigma_3} \tag{4}$$

where $b = 0$ and $b = 1$ represent the triaxial compression and triaxial extension, respectively.

In this study, σ_3 represented the fracture-normal stress, and both σ_1 and σ_2 represented the fracture-lateral stresses. Thus, b contained not only the stress difference between the three principal stresses, but also that between the fracture-lateral and normal stresses. The stress difference ($\sigma_2 - \sigma_3$) in σ_2 and σ_3 directions gradually increased with increasing b and became closer to the stress difference ($\sigma_1 - \sigma_3$) in σ_1 and σ_3 directions. The permeability of the AFS clearly decreases with increasing p, as shown in Fig. 7a, which indicates that the single fracture – as the main fluid flow channel – is compressed and closed. The permeability evolution exhibited a rapid decline followed by a slow decline as p increased, which was likely because the single fracture inside the AFS had been compacted more significantly due to the higher mean stress. Furthermore, the permeability varied at the same mean stress for two reasons:

(1) The permeability displayed a decreasing trend with increasing fracture-normal stress (σ_3). This permeability response indicated that fluid flow in the fracture was dominated by the direct compressive effect of normal stress.
(2) Permeability decreased with increasing intermediate principal stress coefficient when p and the fracture-normal stress were kept constant, because the effect of the fracture-lateral stress (σ_2) on the rock fracture permeability increased with increasing values of b. Thus, the permeability of rocks containing fractures was related not only to the mean stress, but also to the relative magnitude of the three principal stresses.

As shown in Fig. 7b, permeability decreases with increasing intermediate principal stress coefficient at different fracture-normal stresses, which is ascribed to the closure effect of the fracture-lateral stress on the single fracture seepage channel. At low-normal stresses, permeability was characterized by a rapid decrease with increasing b value, indicating an easily compressed fracture and a high variation in fracture aperture. At high-normal stresses, permeability changes were relatively less sensitive to b, demonstrating that the high degree of fracture compaction rendered the fracture difficult to deform and compress. In other words, fracture permeability was impacted by fracture-normal stress in the mean stress, while fracture-lateral stress determined by b similarly caused a decrease in permeability.

4. Discussion

4.1. Determination of fracture normal stiffness

The fracture normal stiffness that characterized fracture deformability was directly related to fracture aperture and thereby also to permeability evolution (Li et al., 2021a). We used the conservation of energy through the principle of virtual work to measure fracture normal stiffness. The external work W_{ext} was equal to the internal work W_{int} associated with the fracture. In order to separate matrix deformation from fracture deformation, the work performed by the external stress W_{ext} can be written as

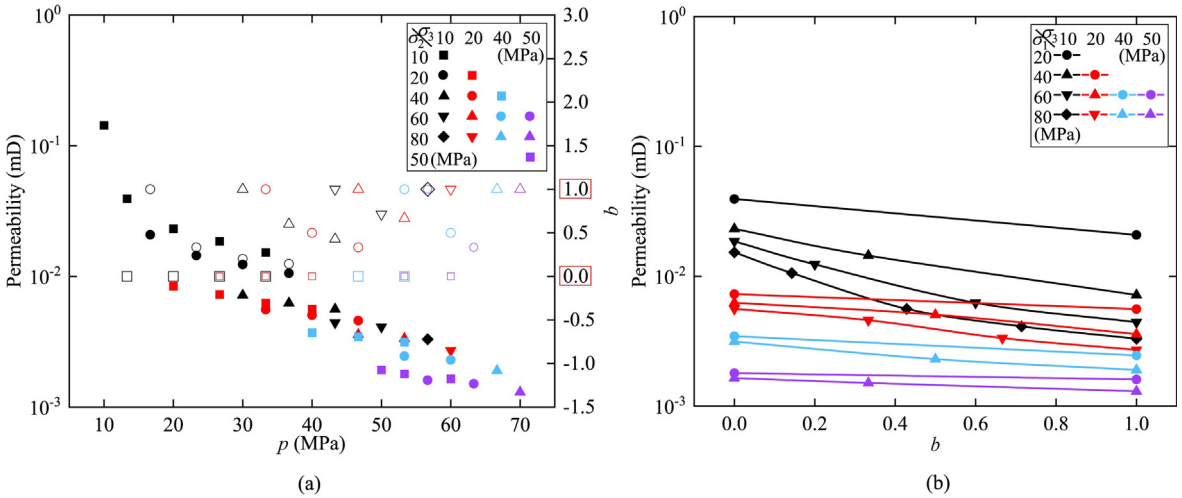

Fig. 7. Relationship between permeability and mean stress and intermediate principal stress coefficient for different 3D stress conditions: (a) Permeability and b as a function of p, and (b) permeability as a function of b. Solid symbols and solid line: permeability under different stress conditions; open symbols: b under stress conditions corresponding to the solid symbols.

$$W_{ext} = \left(F_1^{AFS}\Delta L_1^{AFS} + F_2^{AFS}\Delta L_2^{AFS} + F_3^{AFS}\Delta L_3^{AFS}\right) - \left(F_1^{IS}\Delta L_1^{IS} + F_2^{IS}\Delta L_2^{IS} + F_3^{IS}\Delta L_3^{IS}\right) \quad (5)$$

where F_1^{AFS}, F_2^{AFS}, and F_3^{AFS} are the forces in the directions of σ_1, σ_2, and σ_3, respectively, for the AFS; ΔL_1^{AFS}, ΔL_2^{AFS}, and ΔL_3^{AFS} are the deformations in the directions of σ_1, σ_2, and σ_3, respectively, for the AFS; F_1^{IS}, F_2^{IS}, and F_3^{IS} are the forces in the directions of σ_1, σ_2, and σ_3, respectively, for the IS at same stress conditions corresponding to AFS; and ΔL_1^{IS}, ΔL_2^{IS}, and ΔL_3^{IS} are the deformations in the directions of σ_1, σ_2, and σ_3, respectively, for the IS at same stress conditions corresponding to AFS.

The fracture stiffness K_n was calculated by (Pyrak-Nolte and Morris, 2000; Thörn et al., 2014; Li et al., 2021a):

$$K_n = \frac{\Delta\sigma_n}{\Delta b} \quad (6)$$

where $\Delta\sigma_n$ is the change in the normal stress of the fracture, and Δb is the change in the mechanical aperture of the fracture.

Guidelines for indirect normal stiffness measurements by accounting for intact rock deformation at varying levels of applied normal stress – which have been presented in previous studies (Packulak et al., 2021) – were referenced in the present study. The normal deformation of the IS at the same stress conditions was then subtracted from the normal deformation of the AFS. This determines the change in the fracture mechanical aperture (Fig. 8), which then facilitates measurement of the fracture normal stiffness.

The work performed by the internal fracture W_{int} can be described as

$$W_{int} = K_n A_f \Delta b^2 \quad (7)$$

where K_n is the fracture stiffness, and A_f is the area of the fracture surface.

Combining Eqs. (5) and (7), we have

$$K_n A_f \Delta b^2 = \sum_{i=1}^{3} F_i^{AFS}\Delta L_i^{AFS} - \sum_{i=1}^{3} F_i^{IS}\Delta L_i^{IS} \ (i = 1,2,3) \quad (8)$$

Eq. (8) can be re-written as

$$K_n = \frac{\sum_{i=1}^{3} F_i^{AFS}\Delta L_i^{AFS} - \sum_{i=1}^{3} F_i^{IS}\Delta L_i^{IS}}{A_f \Delta b^2} \ (i = 1,2,3) \quad (9)$$

The stiffness magnitudes measured in the present study are compared with previous experimental data, as shown in Fig. 9. These previous studies (Pyrak-Nolte and Morris, 2000; Li et al., 2021a) focused on the impact of merely applied normal stress on fracture deformation and seepage properties. However, the present study investigated the impact of (relatively) high fracture-normal stress (10–50 MPa) and high fracture-lateral stress (10–80 MPa)

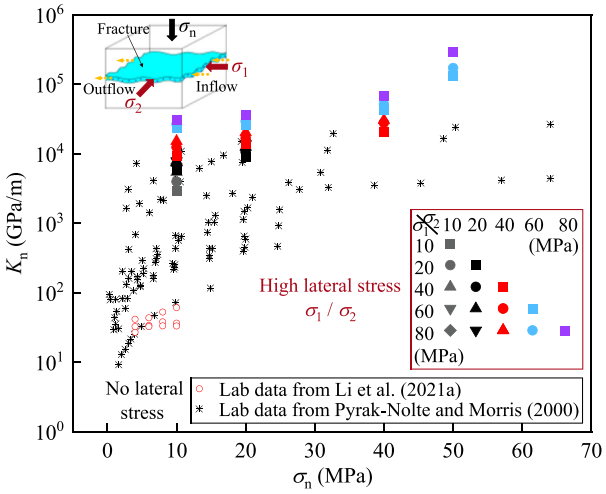

Fig. 9. Comparison of normal stiffness between the present study and other data sources under different stress conditions.

on fracture deformation and permeability, for which no data are known to be available thus far. As illustrated in Fig. 9, the normal stiffness K_n increases with increasing applied fracture-normal stress σ_n. However, the existence of lateral stress allowed for greater variation in fracture normal stiffness, even at the same normal stress. In Fig. 9, the normal stiffness of AFS can be seen to have ranged from between 10^3 GPa/m and 10^6 GPa/m, which is one to two orders of magnitude higher than the stiffness previously obtained under no lateral stress conditions. This finding can be explained by the fact that the fracture had been exposed to additional high lateral stresses and that the adjacent surfaces of the fracture had a significant contact, thereby causing the fracture to be stiffer.

4.2. Relationship between fracture normal stiffness and permeability

The transmissivity $Q/\Delta H$ (Li et al., 2021a) – which was related to permeability – under all experimental conditions were calculated as

$$\frac{Q}{\Delta H} = \frac{k\gamma A_1}{\mu L} \quad (10)$$

where γ is the specific weight of the fluid.

Fig. 10 presents the relationship between $Q/\Delta H$ and K_n, which enabled a comparison with previous studies (Pyrak-Nolte and Morris, 2000; Thörn et al., 2014; Li et al., 2021a). As shown in Fig. 10, normal stiffness K_n increases with increasing applied stress and decreasing permeability. As can be seen in the figure, the normal stiffnesses in previous studies are concentrated on the low-stiffness region, which ranges from between 10 GPa/m and 10^5 GPa/m. In contrast, we measured high normal stiffnesses, which were

Fig. 8. Schematic illustration of obtaining a change in the fracture mechanical aperture.

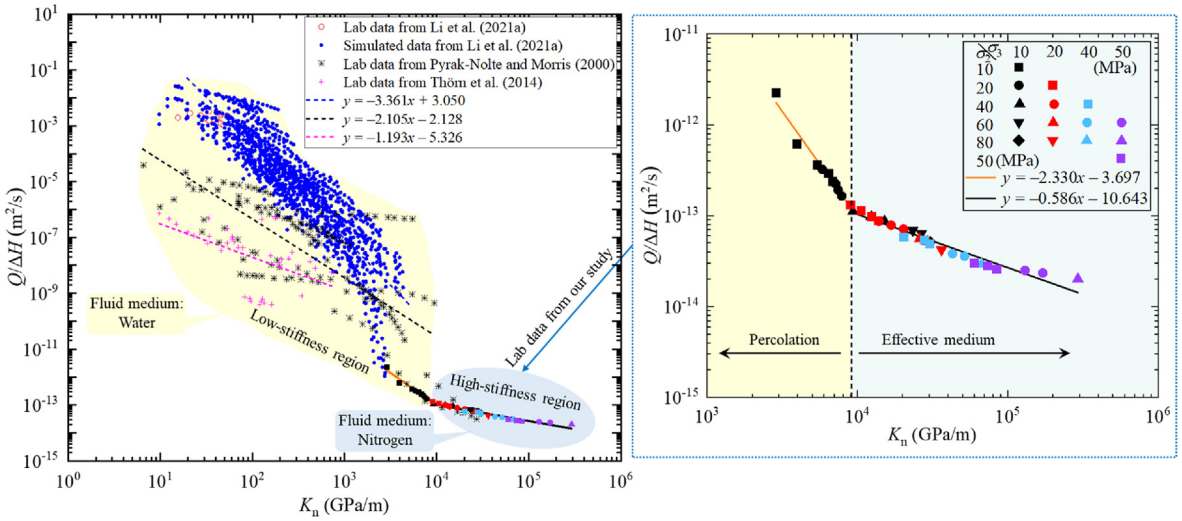

Fig. 10. Relationship between $Q/\Delta H$ and K_n, and comparisons with data from other sources.

firmly located within a low-permeability region. The high lateral stress-induced fracture closure characteristic was consistent with the general trend of low stiffness for large-aperture fractures and high stiffness for low-aperture fractures (Thörn et al., 2014).

The inclination of the curve (Fig. 10) represents the sensitivity of $Q/\Delta H$ to K_n, which is inversely proportional to the degree of matching of the mated fracture surfaces (Li et al., 2021a). The relationship between stiffness and permeability measured in the present study exhibited a lower inclination compared with that of previous studies (Li et al., 2021a), while (Li et al., 2021a)'s study featured the highest inclination and represented an unmated fracture in which the surfaces only poorly fit one another. Data (Pyrak-Nolte and Morris, 2000; Thörn et al., 2014) from samples of a well-mated fracture similar to AFS — in which the surfaces fit one another well — revealed inclinations resembling previous section with larger inclinations than those in latter section in this study. It should be noted that previous studies used water as the fluid medium to measure permeability, whereas in the present study, gas (nitrogen) was used as the fluid medium. The sample concerned here might have been regarded as non-permeable or as having required higher fluid injection pressure if it had been tested with water. This observation further indicates that the fracture was subjected to high 3D stress and that the relative closure of the fracture was more significant, thereby allowing for an extremely small fracture aperture. This finding indicates that:

(1) Fracture normal stiffness approached the limit (over 10^5 GPa/m) as the fracture progressively closed under high fracture-normal and lateral stresses.
(2) Permeability was difficult to further reduce once the flow had become concentrated in a few isolated flow channels within the fracture and as a result of the overall aperture reduction.

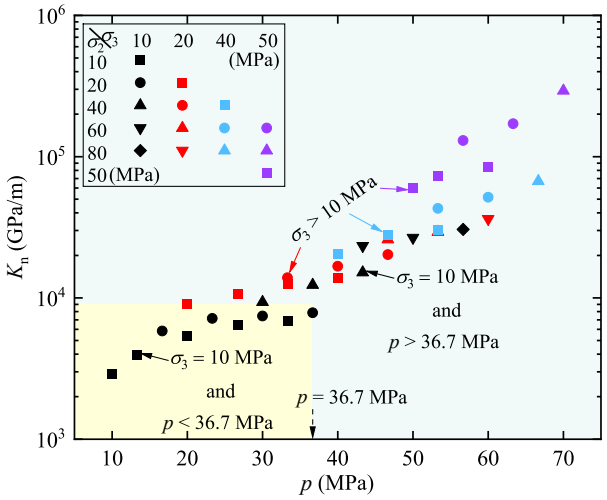

Fig. 11. Relationship between K_n and p.

The work described in the present paper expands on existing knowledge of the relationship between permeability and normal stiffness from the low-stiffness, high-permeability region to the high-stiffness, low-permeability region by using a smooth fracture under applied high lateral stress based on normal stress. The subplot of Fig. 10 displays two regimes with distinct slopes that represent the percolation regime in the low-stiffness, high-permeability region and effective medium regime in high-stiffness, low-permeability region in our study. At $K_n \approx 10^4$ GPa/m, the break-point in the slope was found. The slope of the curve was −2.330 for $K_n < 10^4$ GPa/m (percolation regime) and −0.586 for $K_n > 10^4$ GPa/m (effective medium regime). In order to define the boundaries of the stress range, we characterize the magnitudes of two fracture-lateral stresses (σ_1 and σ_2) based on fracture-normal stress (σ_3) via the mean stress p in Eq. (3) and demonstrate the relationships between p and K_n, as shown in Fig. 11. In the percolation regime, when the fracture-normal and lateral stresses are small ($\sigma_3 = 10$ MPa and $p < 36.7$ MPa), the flow within the fracture is relatively homogeneous and occurs as a multi-channel channelized flow (see Fig. 13b), with permeability being sensitive to small changes in stress. As the stress increased, the flow path progressively closed, and the flow began to become heterogeneous up to normal and lateral stresses associated with the break in the slope of the curve. The above-described stress conditions associated with the effective medium regime were as follows: (1) low normal stress and high lateral stress ($\sigma_3 = 10$ MPa and $p > 36.7$ MPa), and (2) high normal stress supplemented by lateral stress ($\sigma_3 > 10$ MPa). In the effective medium regime, the fracture contains only a few isolated flow channels and exhibits an isolated channelized flow pattern (see Fig. 13b), with permeability being insensitive to stress state. Thus, the change in slope under high 3D

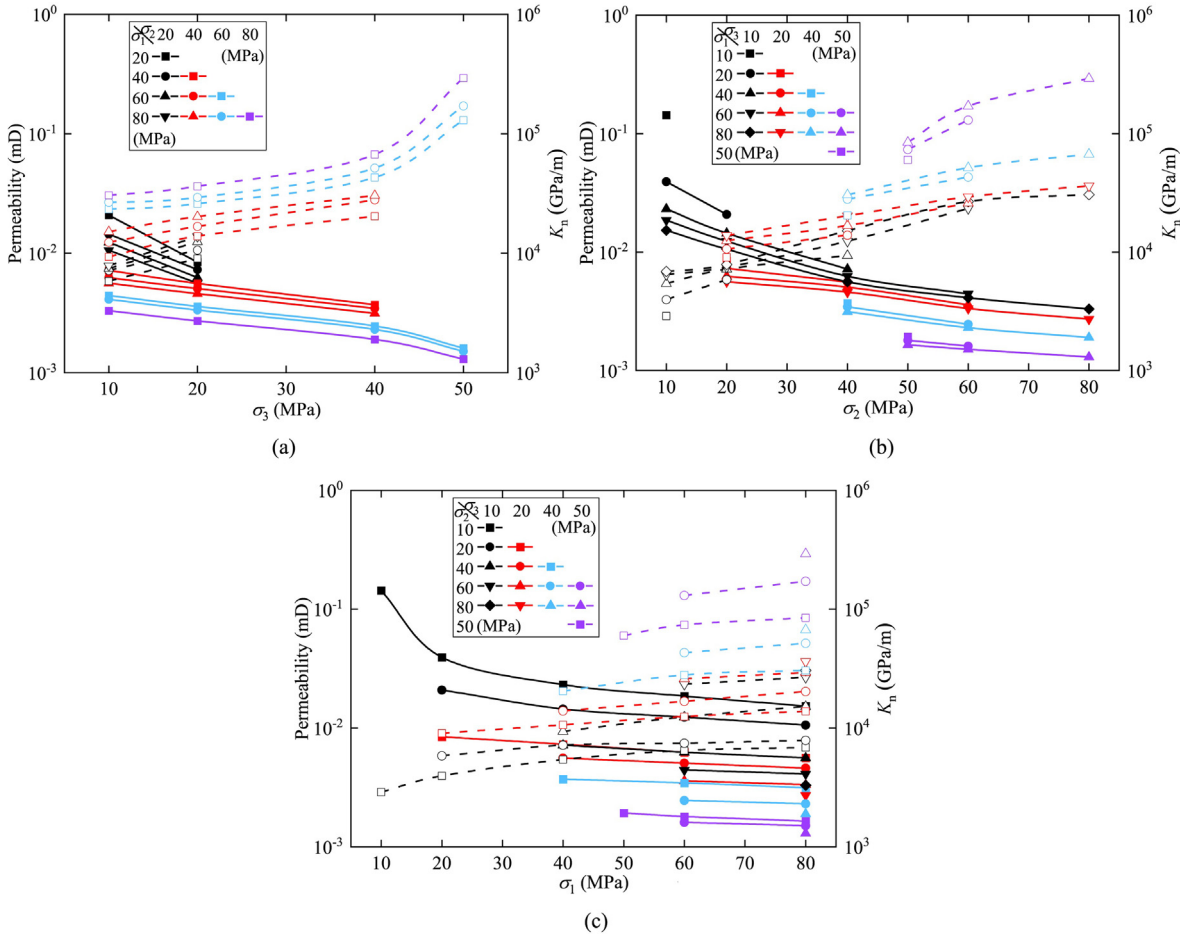

Fig. 12. Fracture normal stiffness and permeability as a function of fracture-lateral stress and fracture-normal stress: (a) Fracture stiffness and permeability as a function of σ_3, (b) fracture stiffness and permeability as a function of σ_2, and (c) fracture stiffness and permeability as a function of σ_1. Solid symbols and solid line: permeability under different stress conditions; open symbols and dashed line: fracture stiffness under stress conditions that correspond to the solid symbols.

stress was associated with a fundamental change in the flow path, as discussed by Pyrak-Nolte and Nolte (2016).

As compared with normal stress, the lateral stress dominated the deformation and flow of the fracture at lower normal stress and additionally played a supplementary role at higher normal stress. According to the stress range that determines the shift of the flow regime in the fracture as shown in Fig. 11, the mechanism of lateral and normal stresses that affect the deformation and flow is as follows:

(1) When the normal stress was low ($\sigma_3 = 10$ MPa), the lateral stress dominated the closure behavior of the fracture, which allowed for a shift in the flow regime (with a boundary of $p = 36.7$ MPa), thereby increasing stiffness and decreasing permeability.
(2) Higher normal stress ($\sigma_3 > 10$ MPa) dominated the deformation and flow behavior of the fracture, with lateral stress as a supplementary factor exacerbating fracture closure. The effect of fracture-lateral stress on the mechanical behavior and fluid-flow characteristics of fractures cannot be ignored.

4.3. Fracture normal stiffness and permeability evolution

In the present study, we expanded the range of measured normal stiffness and permeability beyond that in Fig. 10 using a smooth fracture under high stress. The impact of high fracture-lateral (σ_1 and σ_2) and fracture-normal (σ_3) stresses on normal stiffness and permeability are investigated, and results are illustrated in Fig. 12. Previous studies (e.g. Li et al., 2021a; Packulak et al., 2021) have found that the normal deformation of fractures is caused by the effect of fracture-normal stress while normal stiffness determines the opening and closing of the fracture. In general, normal stiffness has been found to increase with increasing fracture-normal stress. Fig. 12a reveals that normal stiffness increases with increasing σ_3 while permeability decreases, indicating that σ_3 can compress the fracture. Moreover, normal stiffness was also affected by fracture-lateral stresses (σ_1 and σ_2). Fig. 12b and c demonstrates that normal stiffness increases with increasing σ_2 and σ_1 and is accompanied by decrease in the reduction rate of permeability. The fracture-lateral stress featured the same fracture compression closure effect as the normal stress and thus further increased the fracture normal stiffness. Fracture closure that had been caused by increased triaxial stresses explained the increased normal stiffness and decreased permeability. Similarly, the permeability of coal that contained fractures and beddings also exhibited significant stress dependence (Lu et al., 2019a). The stress-induced increase in fracture normal stiffness illustrated reduction in the fracture deformability and compressibility, which was essential for the change in the degree of fracture permeability reduction with increasing stress. The fracture became increasingly difficult to deform as the fracture progressively closed under high stresses, and fluid-flow

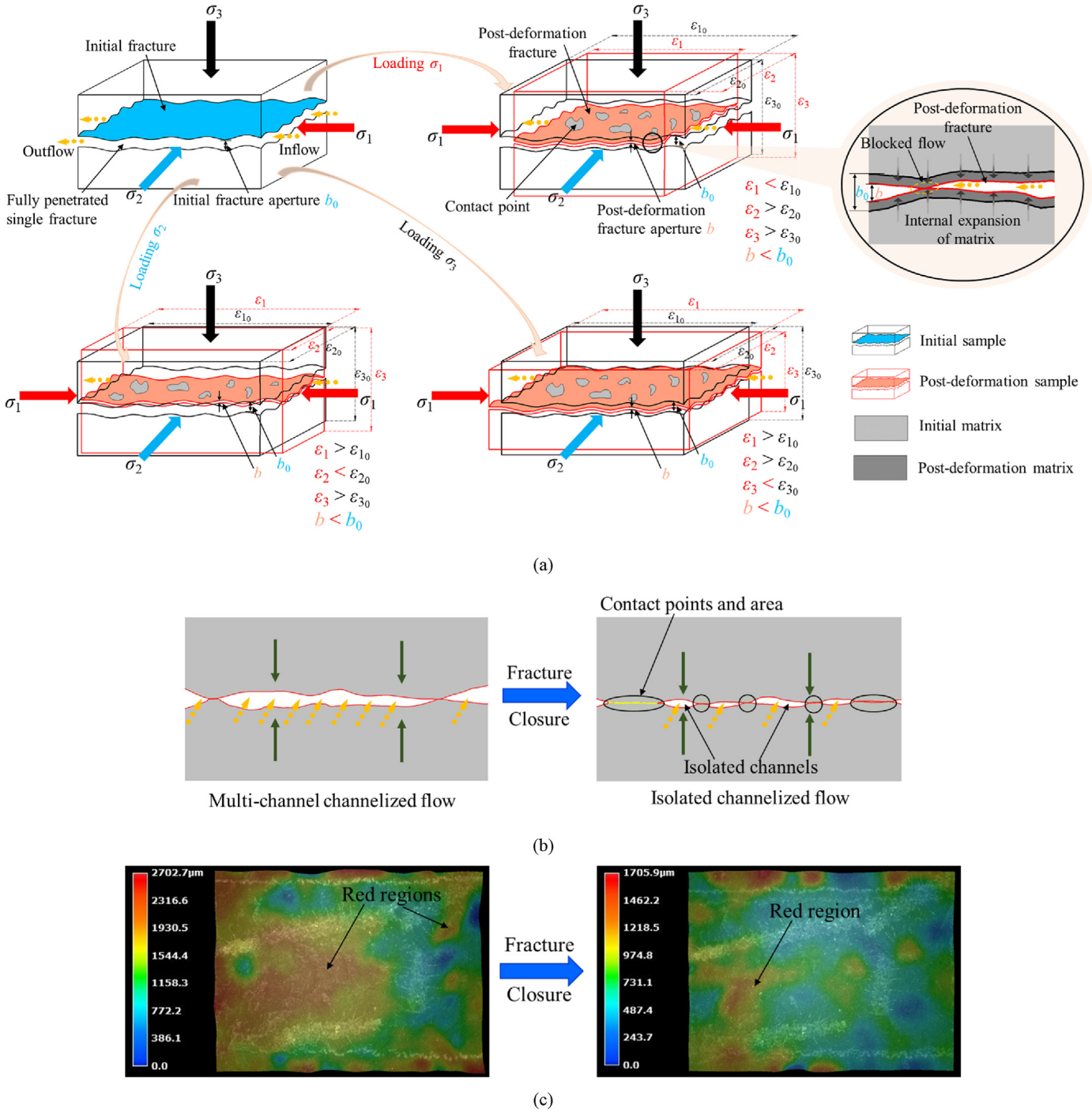

Fig. 13. Schematic of matrix and fracture deformations of the sample under true-triaxial stress conditions: (a) Matrix and fracture deformations, (b) fracture morphology in different fluid-flow states under compression, and (c) fracture surface topography at pre- and post-test. ε_{10}, ε_{20}, and ε_{30} are the initial maximum, intermediate, and minimum principal strains, respectively.

rates within the fracture were reduced by the overall narrowing of the aperture.

4.4. Mechanism of permeability evolution and fracture deformation

Fig. 13a presents a schematic of the matrix and fracture deformations of the sample for change in fracture stiffness caused by increasing triaxial stresses. The shale matrix was compressed in σ_1 direction and expanded in σ_2 and σ_3 directions during loading by σ_1. Furthermore, the fracture was compressed and closed due to the internal expansion of the matrix. Similarly, during σ_2 loading process, matrix-internal expansion and deformation occurred primarily in σ_3 direction, which caused the compression of the fracture. Thus, under the lateral stresses (σ_1 and σ_2), part of the shale matrix expanded outward, which was manifest as a normal expansion of the sample; another part of the shale matrix expanded into the fracture, which caused compression of the fracture due to the Poisson effect. During loading under normal stress (σ_3), the

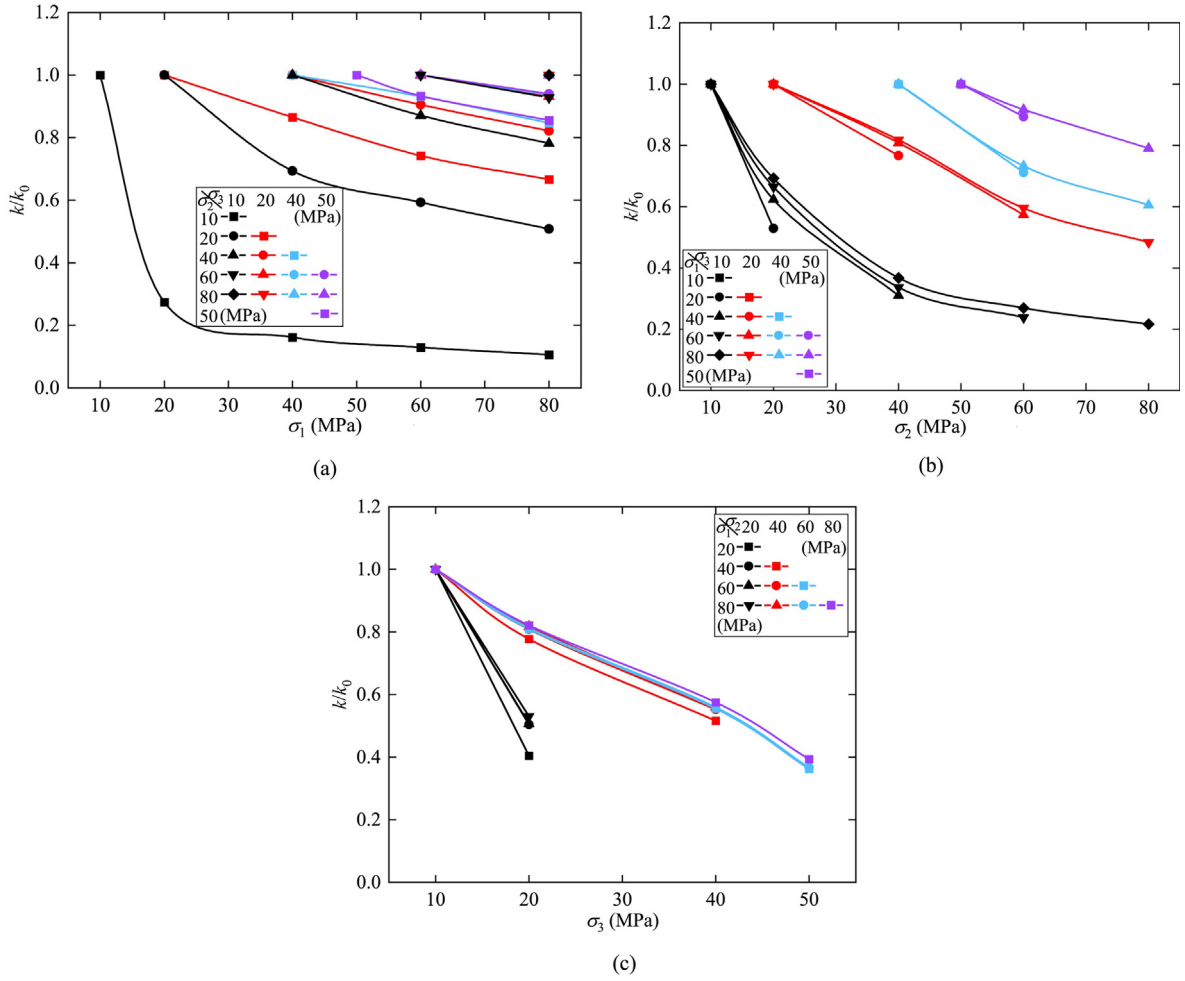

Fig. 14. Relationships between normalized permeability (k/k_0) and σ_3, σ_2, and σ_1 under different stress conditions: (a) Normalized permeability as a function of σ_1, (b) normalized permeability as a function of σ_2, and (c) normalized permeability as a function of σ_3.

adjacent surfaces of the fracture gradually closed under direct compression, which increased fracture normal stiffness and decreased permeability. Therefore, the evolution of permeability was mainly determined by the deformation perpendicular to the fracture. From Fig. 12b and c, when $\sigma_3 = 10$ MPa, fracture stiffness is found to increase from the initial to the final stress state with increasing σ_1 and σ_2 in the range of 14%–138% and 47%–345%, respectively. However, at σ_3 = 20–50 MPa, the increase is only 13%–53% and 31%–247% with increasing σ_1 and σ_2, respectively. This finding indicates that lateral stresses (σ_1 and σ_2) dominate fracture normal deformation at lower normal stress (σ_3). However, higher normal stress (σ_3 increasing from 20 to 50 MPa) dominates fracture normal deformation, and the increase in fracture stiffness is up to 47%–707%, as shown in Fig. 12a.

Both fracture normal stiffness and permeability depended on the aperture and contact area of the adjacent fracture surfaces (Pyrak-Nolte and Morris, 2000). As shown in Fig. 13b, fracture closure under high stress increases the number of fracture contact points as well as their contact area, and simultaneously reduces the fracture aperture. In order to visualize the evolution characteristics of the fracture surface topography under stress changes, the fracture surface zones at pre- and post-test were scanned using a super-depth-of-field 3D optical microscope. As shown in Fig. 13c, the reduction in red regions on the fracture surface induced by fracture compression indicates that fracture closure under increasing triaxial stresses allows for an increase in fracture contact points and area. This resulted in an increase in normal stiffness as well as in a decrease in hydraulic aperture, and thereby in permeability. Deng et al. (2024) proposed a similar law regarding an increase in normal stiffness as permeability decreased for field-scale fractures during closure, and it is verified that such law was strongly related to the effective contact area along the fracture. Flow in fractures was always channelized flow, and the flow state was changed via stress-induced compression as well as via the closure of the flow channels. The fluid-flow state transformed from a relatively homogeneous multi-channel channelized flow to a heterogeneous isolated channelized flow that was concentrated on a few isolated channels.

4.5. Normalized permeability

In order to better evaluate the reduction in permeability with fracture-lateral (σ_1 and σ_2) and fracture-normal (σ_3) stresses, permeability was normalized as k/k_0, with k as the measured permeability and k_0 as the corresponding initial value for each stress condition. Fig. 14 shows the relationships between the normalized permeability (k/k_0) and σ_3, σ_2, and σ_1 under different stress conditions. The decreasing trend in permeability becomes progressively slower with increase in σ_3 for the same increment of σ_1, as shown in Fig. 14a. Similar observations can be noted in Fig. 14b for the same increment in σ_2. This feature has also been observed for fractures in coal and sandstone, as verified by Lu et al. (2019a). In

addition, in the present study, the effect of fracture-normal stress on permeability is clear and plays a dominant role compared with that of lateral stress, as shown in Fig. 14c.

When subjected to an increase in σ_1, the external expansion in σ_3 direction was suppressed by the increased σ_3. For example, the expansion in ε_3 decreased from 0.124‰ at σ_3 = 10 MPa and σ_2 = 60 MPa, to only 0.118‰ at σ_3 = 50 MPa and σ_2 = 60 MPa when σ_1 increased from 60 MPa to 80 MPa. During the loading of σ_2, the external expansion decreased with increasing σ_3. For example, the expansion in ε_3 decreased from 0.18‰ at σ_3 = 10 MPa and σ_1 = 80 MPa to 0.08‰ at σ_3 = 50 MPa and σ_1 = 80 MPa when σ_2 increased from 60 MPa to 80 MPa. The above-described behavior identified the fracture closure that had been caused by the internal expansion of the matrix. As a result, the residual aperture (Thörn et al., 2014) was approached, and both the contact area of fracture surfaces and the fracture stiffness increased, which indicated that the deformability of the fracture had been reduced. The two behaviors became more pronounced with increasing lateral constraint, and thus attenuated the degree of aperture and permeability reduction caused by increasing σ_3, σ_2, or σ_1.

5. Conclusions

The present study measured the permeability evolution and deformation characteristics of fractured shale under true-triaxial stress conditions. A relationship between permeability and fracture normal stiffness was proposed based on the principle of virtual work. The effects of fracture-lateral and fracture-normal stresses on fracture permeability, normal stiffness, and the deformation mechanisms of the rock were analyzed and discussed. In this work, the following conclusions were drawn:

(1) The permeability of artificially fractured shale decreased with increasing mean stress and intermediate principal stress coefficients. When the mean stress was constant, the fluid flow in the fracture was dominated by the direct compressive effect of fracture-normal stress. However, the Poisson effect — which was induced via fracture-lateral stress as determined by an intermediate principal stress coefficient — further reduced permeability with constant mean stress and normal stress.

(2) The fracture normal stiffness of the fractured rock was not only dominated by normal stress, but also exhibited a positive correlation with lateral stresses. The contact area of the fracture surface was found to be proportional to the loading stress, which resulted in increased normal stiffness with increased contact. This observation was illustrated by the decrease in fracture deformability and compressibility (and by the increase in stiffness) with increasing stress, which is critical when it comes to predicting fracture permeability reduction.

(3) We experimentally determined the relationship between permeability and normal stiffness beyond the low-stiffness, high-permeability region and into the high-stiffness, low-permeability region under (relatively) high fracture-normal and lateral stress conditions. As high fracture-lateral stress increased, the fracture progressively closed together with normal stiffness far beyond the stiffness previously reported under no lateral stress conditions ($>10^5$ GPa/m). The presence of lateral stresses reduced the influence of both fracture deformability and the reduction in permeability with stress. This event captured a fundamental change in flow path topology as the flow field morphed from a multi-channel to an isolated channelized flow.

(4) Compared with normal stress, lateral stress dominated the closure behavior of fractures at lower normal stress (σ_3 = 10 MPa), which allowed for a shift in the flow regime, thereby increasing normal stiffness and decreasing permeability. Higher normal stress (σ_3 > 10 MPa) dominated the deformation and flow behavior of the fracture, with lateral stress serving as a supplementary factor that exacerbated fracture closure. The effect of fracture-lateral stress on the mechanical behavior and fluid-flow characteristics of fractures cannot be ignored.

However, there were limitations in this work:

(1) The establishment of the fracture normal stiffness—permeability relations can aid in assessing the hydro-mechanical coupling of fractures in the crust. However, previous studies have only considered fracture-normal stress to directly measure normal stiffness, and the effect of fracture-lateral stresses has been largely ignored in the evaluation of normal stiffness. To accommodate these needs, we proposed a method for measuring fracture normal stiffness that considers the effects of fracture-lateral and fracture-normal stresses on the stiffness—permeability relations in this study. The stiffness—permeability relations are also related to the fracture surface roughness, although our study is limited to being based on the same fracture, whereas a pair of fractures can only provide a certain pattern of surface geometry.

(2) Thus, future work should also consider a series of true-triaxial stress-permeability tests for fractures with different roughness to investigate and quantify the elusive relationships between fracture stiffness—permeability for different surface roughness coefficients at high triaxial stresses. In addition, permeability evolution is influenced by time-dependent deformation. Therefore, the fracture surface roughness should also be considered together with impact of related time effects. Furthermore, the microstructural mechanism of permeability hysteresis could require further research. This behavior would be the irrecoverable plastic deformation at the contact points between the fracture surfaces, resulting in the permeability hysteresis.

CRediT authorship contribution statement

Fudong Li: Conceptualization, Data curation, Formal analysis, Investigation, Methodology, Validation, Visualization, Writing — original draft. **Derek Elsworth:** Conceptualization, Formal analysis, Investigation, Methodology, Supervision, Validation, Visualization, Writing — review & editing. **Xia-Ting Feng:** Conceptualization, Formal analysis, Investigation, Methodology, Resources, Software, Supervision, Visualization, Writing — review & editing. **Tianyu Chen:** Conceptualization, Data curation, Funding acquisition, Methodology, Project administration, Resources, Supervision, Validation, Writing — review & editing, Formal analysis. **Jun Zhao:** Formal analysis, Resources, Software, Visualization. **Yingchun Li:** Methodology, Validation, Writing — review & editing. **Jianyu Zhang:** Investigation, Project administration, Resources. **Qiong Wu:** Formal analysis, Project administration, Resources. **Guanglei Cui:** Conceptualization, Formal analysis, Investigation, Methodology, Validation, Visualization, Writing — review & editing.

Declaration of competing interest

The authors declare that they have no known competing

financial interests or personal relationships that could have appeared to influence the work reported in this paper.

Acknowledgments

This work is funded by the joint fund of the National Key Research and Development Program of China (Grant No. 2021YFC2902101), National Natural Science Foundation of China (Grant No. 52374084), and the 111 Project (Grant No. B17009). DE acknowledges support from the G. Albert Shoemaker endowment. The authors would like to thank Pr. Haikuan Nie from State Key Laboratory of Shale Oil and Gas Enrichment Mechanisms and Effective Development for providing permission to use Fig. 2a in this paper. The authors would like to thank the reviewers for their valuable comments and suggestions that helped improve this paper.

References

Anderson, E.M., 1905. The dynamics of faulting. Trans. Edinb. Geol. Soc. 8 (3), 387–402.
Bandis, S.C., Lumsden, A.C., Barton, N.R., 1983. Fundamentals of rock joint deformation. Int. J. Rock Mech. Min. Sci. Geomech. Abstr. 20 (6), 249–268.
Barton, N., 2020. A review of mechanical over-closure and thermal over-closure of rock joints: potential consequences for coupled modelling of nuclear waste disposal and geothermal energy development. Tunn. Undergr. Space Technol. 99, 103379.
Barton, N., Bandis, S., Bakhtar, K., 1985. Strength, deformation and conductivity coupling of rock joints. Int. J. Rock Mech. Min. Sci. Geomech. Abstr. 22 (3), 121–140.
Brace, W.F., Walsh, J.B., Frangos, W.T., 1968. Permeability of granite under high pressure. J. Geophys. Res. 73 (6), 2225–2236.
Cappa, F., Guglielmi, Y., Rutqvist, J., Tsang, C.F., Thoraval, A., 2008. Estimation of fracture flow parameters through numerical analysis of hydromechanical pressure pulses. Water Resour. Res. 44 (11), W11408.
Carey, J.W., Lei, Z., Rougier, E., Mori, H., Viswanathan, H., 2015. Fracture-permeability behavior of shale. J. Unconv. Oil Gas Resour. 11, 27–43.
Chen, D., Pan, Z., Ye, Z., 2015. Dependence of gas shale fracture permeability on effective stress and reservoir pressure: model match and insights. Fuel 139, 383–392.
Chen, T., Feng, X.T., Cui, G., Tan, Y., Pan, Z., 2019a. Experimental study of permeability change of organic-rich gas shales under high effective stress. J. Nat. Gas Sci. Eng. 64, 1–14.
Chen, T., Fu, Y., Feng, X.T., Tan, Y., Cui, G., Elsworth, D., Pan, Z., 2021. Gas permeability and fracture compressibility for proppant-supported shale fractures under high stress. J. Nat. Gas Sci. Eng. 95, 104157.
Chen, T.Y., Hao, Y.Y., Elsworth, D., Zhang, H.M., Hu, Z.M., Cui, G.L., 2023. Modes of multi-mechanistic gas diffusion in shale matrix at varied effective stresses: observations and analysis. Petrol. Sci. 20 (5), 2908–2920.
Chen, Y., Jiang, C., Yin, G., Zhang, D., Xing, H., Wei, A., 2019b. Permeability evolution under true triaxial stress conditions of Longmaxi shale in the Sichuan Basin, Southwest China. Powder Technol. 354, 601–614.
Cho, Y., Apaydin, O.G., Ozkan, E., 2013. Pressure-dependent natural-fracture permeability in shale and its effect on shale-gas well production. SPE Reserv. Eval. Eng. 16 (2), 216–228.
Choi, M.K., Bobet, A., Pyrak-Nolte, L.J., 2014. The effect of surface roughness and mixed-mode loading on the stiffness ratio κ_x/κ_z for fractures. Geophys 79 (5), D319–D331.
Cui, G., Feng, X.T., Pan, Z., Chen, T., Liu, J., Elsworth, D., Tan, Y., Wang, C., 2020b. Impact of shale matrix mechanical interactions on gas transport during production. J. Pet. Sci. Eng. 184, 106524.
Cui, G., Liu, J., Wei, M., Shi, Y., Elsworth, D., 2018. Why shale permeability changes under variable effective stresses: new insights. Fuel 213, 55–71.
Cui, G., Tan, Y., Chen, T., Feng, X.T., Elsworth, D., Pan, Z., Wang, C., 2020a. Multi-domain two-phase flow model to study the impacts of hydraulic fracturing on shale gas production. Energy Fuel. 34 (4), 4273–4288.
Cui, L., Zhang, F., An, M., Zhong, Z., Wang, H., 2024. Frictional stability and permeability evolution of 3D carved Longmaxi shale fractures and its implications for shale fault stability in Sichuan Basin. Rock Mech. Rock Eng. 57, 5415–5430.
Deng, Q., Schmittbuhl, J., Cacace, M., Blöcher, G., 2024. Mechanical stiffness and permeability of a reservoir-scale rough fracture during closure. J. Geophys. Res. Solid Earth 129 (9), e2024JB029001.
Dong, J.J., Hsu, J.Y., Wu, W.J., Shimamoto, T., Hung, J.H., Yeh, E.C., Wu, Y.H., Sone, H., 2010. Stress-dependence of the permeability and porosity of sandstone and shale from TCDP Hole-A. Int. J. Rock Mech. Min. Sci. 47 (7), 1141–1157.
Ellsworth, W.L., Giardini, D., Townend, J., Ge, S., Shimamoto, T., 2019. Triggering of the Pohang, Korea, earthquake (M_w 5.5) by enhanced geothermal system stimulation. Seismol Res. Lett. 90 (5), 1844–1858.
Fan, Z., Eichhubl, P., Newell, P., 2019. Basement fault reactivation by fluid injection into sedimentary reservoirs: poroelastic effects. J. Geophys. Res. Solid Earth 124 (7), 7354–7369.
Feng, X.T., Zhao, J., Zhang, X., Kong, R., 2018. A novel true triaxial apparatus for studying the time-dependent behaviour of hard rocks under high stress. Rock Mech. Rock Eng. 51 (9), 2653–2667.
Frash, L.P., Carey, J.W., Lei, Z., Rougier, E., Ickes, T., Viswanathan, H.S., 2016. High-stress triaxial direct-shear fracturing of Utica shale and in situ X-ray microtomography with permeability measurement. J. Geophys. Res. Solid Earth 121 (7), 5493–5508.
Guglielmi, Y., Mudry, J., 2001. Quantitative measurement of channel-block hydraulic interactions by experimental saturation of a large, natural, fissured rock mass. Ground Water 39 (5), 696–701.
Gutierrez, M., Øino, L.E., Nygård, R., 2000. Stress-dependent permeability of a demineralised fracture in shale. Mar. Petrol. Geol. 17 (8), 895–907.
Haimson, B.C., Chang, C., 2002. True triaxial strength of the KTB amphibolite under borehole wall conditions and its use to estimate the maximum horizontal in situ stress. J. Geophys. Res. Solid Earth 107 (B10). ETG 15-1–ETG 15-14.
Jia, Y., Fang, Y., Elsworth, D., Wu, W., 2020. Slip velocity dependence of friction-permeability response of shale fractures. Rock Mech. Rock Eng. 53 (5), 2109–2121.
Jia, Y., Lu, Z., Xiong, Q., Hampton, J.C., Zhang, Y., He, P., 2021. Laboratory characterization of cyclic hydraulic fracturing for deep shale application in Southwest China. Int. J. Rock Mech. Min. Sci. 148, 104945.
Jiang, T., Yao, W., Sun, X., Qi, C., Li, X., Xia, K., Zhang, J., Nasseri, M.H.B., 2021. Evolution of anisotropic permeability of fractured sandstones subjected to true-triaxial stresses during reservoir depletion. J. Pet. Sci. Eng. 200, 108251.
Jiang, X.W., Wan, L., Wang, X.S., Liang, S.H., Hu, B.X., 2009. Estimation of fracture normal stiffness using a transmissivity-depth correlation. Int. J. Rock Mech. Min. Sci. 46 (1), 51–58.
Johnson, T.C., Burghardt, J., Strickland, C., Knox, H., Vermeul, V., White, M., Schwering, P., Blankenship, D., Kneafsey, T., 2021. 4D proxy imaging of fracture dilation and stress shadowing using electrical resistivity tomography during high pressure injections into a dense rock formation. J. Geophys. Res. Solid Earth 126 (11), e2021JB022298.
Johnson, T.C., Burghardt, J., Strickland, C., Sirota, D., Vermeul, V., Knox, H., Schwering, P., Blankenship, D., Kneafsey, T., 2024. 4D electrical resistivity imaging of stress perturbations induced during high-pressure shear stimulation tests. Geophys. Res. Lett. 51 (10), e2024GL108423.
Kruszewski, M., Montegrossi, G., Parisio, F., Saenger, E.H., 2022. Borehole observation-based in situ stress state estimation of the Los Humeros geothermal field (Mexico). Geomech. Energy Environ. 32, 100392.
Lei, Q., Barton, N., 2022. On the selection of joint constitutive models for geomechanics simulation of fractured rocks. Comput. Geotech. 145, 104707.
Li, B., Cui, X., Zou, L., Cvetkovic, V., 2021a. On the relationship between normal stiffness and permeability of rock fractures. Geophys. Res. Lett. 48 (20), e2021GL095593.
Li, B., Jiang, Y., Koyama, T., Jing, L., Tanabashi, Y., 2008. Experimental study of the hydro-mechanical behavior of rock joints using a parallel-plate model containing contact areas and artificial fractures. Int. J. Rock Mech. Min. Sci. 45 (3), 362–375.
Li, B., Zhao, Z., Jiang, Y., Jing, L., 2015. Contact mechanism of a rock fracture subjected to normal loading and its impact on fast closure behavior during initial stage of fluid flow experiment. Int. J. Numer. Anal. Methods GeoMech. 39 (13), 1431–1449.
Li, M., Liu, X., 2021. Experimental and numerical investigation of the failure mechanism and permeability evolution of sandstone based on hydro-mechanical coupling. J. Nat. Gas Sci. Eng. 95, 104240.
Li, S.Z., Zhou, Z., Nie, H.K., Zhang, L.F., Song, T., Liu, W.B., Li, H.H., Xu, Q.C., Wei, S.Y., Tao, S., 2022. Distribution characteristics, exploration and development, geological theories research progress and exploration directions of shale gas in China. China Geol 5 (1), 110–135.
Li, W., Frash, L.P., Welch, N.J., Carey, J.W., Meng, M., Wigand, M., 2021b. Stress-dependent fracture permeability measurements and implications for shale gas production. Fuel 290, 119984.
Liu, H.H., Rutqvist, J., Berryman, J.G., 2009. On the relationship between stress and elastic strain for porous and fractured rock. Int. J. Rock Mech. Min. Sci. 46 (2), 289–296.
Liu, J., Xue, Y., Zhang, Q., Wang, H., Wang, S., 2022. Coupled thermo-hydro-mechanical modelling for geothermal doublet system with 3D fractal fracture. Appl. Therm. Eng. 200, 117716.
Liu, Q., Li, J., Liang, B., Liu, J., Sun, W., He, J., Lei, Y., 2023. Complex wettability behavior triggering mechanism on imbibition: a model construction and comparative study based on analysis at multiple scales. Energy 275, 127434.
Lu, J., Yin, G., Deng, B., Zhang, W., Li, M., Chai, X., Liu, C., Liu, Y., 2019a. Permeability characteristics of layered composite coal-rock under true triaxial stress conditions. J. Nat. Gas Sci. Eng. 66, 60–76.
Lu, J., Yin, G., Li, X., Li, M., Zhang, D., Zhang, W., Kang, Q., 2019b. Deformation and CO_2 gas permeability response of sandstone to mean and deviatoric stress variations under true triaxial stress conditions. Tunn. Undergr. Space Technol. 84, 259–272.
Ma, Y., Pan, Z., Zhong, N., Connell, L.D., Down, D.I., Lin, W., Zhang, Y., 2016. Experimental study of anisotropic gas permeability and its relationship with fracture structure of Longmaxi Shales, Sichuan Basin, China. Fuel 180, 106–115.
Meng, M., Frash, L.P., Li, W., Welch, N.J., Carey, J.W., Morris, J., Neupane, G., Ulrich, C., Kneafsey, T., 2022. Hydro-mechanical measurements of sheared crystalline rock

fractures with applications for EGS collab experiments 1 and 2. J. Geophys. Res. Solid Earth 127 (2), e2021JB023000.
Nie, H., Li, D., Liu, G., Lu, Z., Wang, H., Wang, R., Zhang, G., 2020. An overview of the geology and production of the Fuling shale gas field, Sichuan Basin, China. Energy Geosci 1 (3–4), 147–164.
Ogata, S., Nishira, E., Yasuhara, H., Kinoshita, N., Inui, T., Kishida, K., 2022. Multi-physics numerical analyses for predicting the alterations in permeability and reactive transport behavior within single rock fractures depending on temperature, stress, and fluid pH conditions. Soils Found. 62 (6), 101207.
Packulak, T.R.M., Day, J.J., Ahmed Labeid, M.T., Diederichs, M.S., 2021. New data processing protocols to isolate fracture deformations to measure normal and shear joint stiffness. Rock Mech. Rock Eng. 55 (5), 2631–2650.
Pan, Z., Ma, Y., Connell, L.D., Down, D.I., Camilleri, M., 2015. Measuring anisotropic permeability using a cubic shale sample in a triaxial cell. J. Nat. Gas Sci. Eng. 26, 336–344.
Petrovitch, C.L., Nolte, D.D., Pyrak-Nolte, L.J., 2013. Scaling of fluid flow versus fracture stiffness. Geophys. Res. Lett. 40 (10), 2076–2080.
Petrovitch, C.L., Pyrak-Nolte, L.J., Nolte, D.D., 2014. Combined scaling of fluid flow and seismic stiffness in single fractures. Rock Mech. Rock Eng. 47 (5), 1613–1623.
Puller, J.W., Mills, K.W., Jeffrey, R.G., Walker, R.J., 2016. In-situ stress measurements and stress change monitoring to monitor overburden caving behaviour and hydraulic fracture pre-conditioning. Int. J. Min. Sci. Technol. 26 (1), 103–110.
Pyrak-Nolte, L.J., 1996. The seismic response of fractures and the interrelations among fracture properties. Int. J. Rock Mech. Min. Sci. Geomech. Abstr. 33 (8), 787–802.
Pyrak-Nolte, L.J., Morris, J.P., 2000. Single fractures under normal stress: the relation between fracture specific stiffness and fluid flow. Int. J. Rock Mech. Min. Sci. 37 (1–2), 245–262.
Pyrak-Nolte, L.J., Nolte, D.D., 2016. Approaching a universal scaling relationship between fracture stiffness and fluid flow. Nat. Commun. 7, 10663.
Raven, K.G., Gale, J.E., 1985. Water flow in a natural rock fracture as a function of stress and sample size. Int. J. Rock Mech. Min. Sci. Geomech. Abstr. 22 (4), 251–261.
Raziperchikolaee, S., Pasumarti, A., 2020. The impact of the depth-dependence of in-situ stresses on the effectiveness of stacked caprock reservoir systems for CO_2 storage. J. Nat. Gas Sci. Eng. 79, 103361.
Rutqvist, J., 1995. Determination of hydraulic normal stiffness of fractures in hard rock from well testing. Int. J. Rock Mech. Min. Sci. Geomech. Abstr. 32 (5), 513–523.
Sun, W., Li, J., Liu, Q., Liang, B., Liu, J., Lei, Y., 2024. Complexity upgrade and triggering mechanism of mixed-wettability: comparative study of CO_2 displacement in different phases. Fuel 369, 131798.
Tan, Y., Pan, Z., Feng, X.T., Zhang, D., Connell, L.D., Li, S., 2019. Laboratory characterisation of fracture compressibility for coal and shale gas reservoir rocks: a review. Int. J. Coal Geol. 204, 1–17.
Tan, Y., Pan, Z., Liu, J., Feng, X.T., Connell, L.D., 2018. Laboratory study of proppant on shale fracture permeability and compressibility. Fuel 222, 83–97.
Tan, Y., Pan, Z., Liu, J., Wu, Y., Haque, A., Connell, L.D., 2017. Experimental study of permeability and its anisotropy for shale fracture supported with proppant. J. Nat. Gas Sci. Eng. 44, 250–264.
Thörn, J., Ericsson, L.O., Fransson, Å., 2014. Hydraulic and hydromechanical laboratory testing of large crystalline rock cores. Rock Mech. Rock Eng. 48 (1), 61–73.
Verdon, J.P., Wüstefeld, A., 2013. Measurement of the normal/tangential fracture compliance ratio (Z_N/Z_T) during hydraulic fracture stimulation using S-wave splitting data. Geophys. Prospect. 61 (Suppl. 1), 461–475.
Walsh, R., McDermott, C., Kolditz, O., 2008. Numerical modeling of stress-permeability coupling in rough fractures. Hydrogeol. J. 16 (4), 613–627.
Wang, L., Cardenas, M.B., 2016. Development of an empirical model relating permeability and specific stiffness for rough fractures from numerical deformation experiments. J. Geophys. Res. Solid Earth 121 (7), 4977–4989.
Xie, H., Lu, J., Li, C., Li, M., Gao, M., 2022. Experimental study on the mechanical and failure behaviors of deep rock subjected to true triaxial stress: a review. Int. J. Min. Sci. Technol. 32 (5), 915–950.
Xue, Y., Teng, T., Dang, F., Ma, Z., Wang, S., Xue, H., 2020. Productivity analysis of fractured wells in reservoir of hydrogen and carbon based on dual-porosity medium model. Int. J. Hydrogen Energy 45 (39), 20240–20249.
Ye, Z., Ghassemi, A., 2019. Injection-Induced Propagation and coalescence of pre-existing fractures in granite under triaxial stress. J. Geophys. Res. Solid Earth 124 (8), 7806–7821.
Ye, Z., Ghassemi, A., 2020. Heterogeneous fracture slip and aseismic-seismic transition in a triaxial injection test. Geophys. Res. Lett. 47 (14), e2020GL087739.
Yong, R., Wu, J., Huang, H., Xu, E., Xu, B., 2022. Complex in situ stress states in a deep shale gas reservoir in the southern Sichuan Basin, China: from field stress measurements to in situ stress modeling. Mar. Petrol. Geol. 141, 105702.
Zhang, Y., Ma, Y., Hu, Z., Lei, H., Bai, L., Lei, Z., Zhang, Q., 2019. An experimental investigation into the characteristics of hydraulic fracturing and fracture permeability after hydraulic fracturing in granite. Renew. Energy 140, 615–624.
Zhao, J., Feng, X.T., Guo, H., Hu, Y., Chen, G., Yang, C., 2022. Time-dependent failure characteristics of excavated rock masses in deep buried engineering: a field case and experimental study. Bull. Eng. Geol. Environ. 81, 520.
Zhao, J., Hu, L., Feng, X.T., Xiao, Y., Guo, Y., 2023. Shear failure mechanisms of sandstone subjected to direct, true-triaxial and confining shear test conditions. Rock Mech. Rock Eng. 56, 6889–6903.
Zhou, J., Zhang, L., Li, X., Pan, Z., 2019. Experimental and modeling study of the stress-dependent permeability of a single fracture in shale under high effective stress. Fuel 257, 116078.
Zimmerman, R.W., Al-Yaarubi, A., Pain, C.C., Grattoni, C.A., 2004. Non-linear regimes of fluid flow in rock fractures. Int. J. Rock Mech. Min. Sci. 41 (3), 384.
Zou, L., Cvetkovic, V., 2020. Impact of normal stress-induced closure on laboratory-scale solute transport in a natural rock fracture. J. Rock Mech. Geotech. Eng. 12 (4), 732–741.

Tianyu Chen obtained her PhD from Northeastern University, China in 2015. She is currently an associate professor at the same university. Her research focuses on the efficiency and safety of unconventional energy extraction. She is the Principal Investigator of several projects including the National Key R&D Program of China, National Natural Science Foundation of China (NSFC), and provincial and ministerial Projects. She has published more than 30 academic papers.